



AMERICAN METEOROLOGICAL SOCIETY

Journal of Climate

EARLY ONLINE RELEASE

This is a preliminary PDF of the author-produced manuscript that has been peer-reviewed and accepted for publication. Since it is being posted so soon after acceptance, it has not yet been copyedited, formatted, or processed by AMS Publications. This preliminary version of the manuscript may be downloaded, distributed, and cited, but please be aware that there will be visual differences and possibly some content differences between this version and the final published version.

The DOI for this manuscript is doi: 10.1175/JCLI-D-11-00610.1

The final published version of this manuscript will replace the preliminary version at the above DOI once it is available.

If you would like to cite this EOR in a separate work, please use the following full citation:

Remillard, J., P. Kollias, E. Luke, and R. Wood, 2012: Marine Boundary Layer Cloud Observations in the Azores. *J. Climate*. doi:10.1175/JCLI-D-11-00610.1, in press.



1
2
3
4
5
6
7
8
9
10
11
12
13
14
15
16
17
18
19
20
21
22
23
24
25
26
27
28

Marine Boundary Layer Cloud Observations in the Azores

Jasmine Rémillard¹, Pavlos Kollias¹, Edward Luke² and Robert Wood³

1. Department of Atmospheric and Oceanic Sciences, McGill University, Montreal QC
2. Atmospheric Sciences Division, Brookhaven National Laboratory, Upton NY
3. Department of Atmospheric Sciences, University of Washington, Seattle WA

Corresponding Author's email: jasmine.remillard@mail.mcgill.ca

Department of Atmospheric and Oceanic Sciences

Room 945, Burnside Hall, 805 Sherbrooke Street West

Montreal, Quebec H3A 2K6

Tel.: 514-398-1500

Fax: 514-398-6115

Abstract

1
2
3
4
5
6
7
8
9
10
11
12
13
14
15
16
17
18
19
20
21
22

The recent deployment of the ARM Mobile Facility at the Graciosa Island, Azores, in the context of the Clouds, Aerosol and Precipitation in the Marine Boundary Layer (CAP-MBL) field campaign added the most extensive (19 months) and comprehensive dataset of MBL clouds to date. Cloud occurrence is high (60–80%) with a summertime minimum. Liquid precipitation is frequently present (30–40%), mainly in the form of virga. Boundary layer clouds are the most frequently observed cloud type (40–50%) with a maximum of occurrence during the summer and fall months under the presence of anticyclonic conditions. Cumulus clouds are the most frequently occurring MBL cloud type (20%), with cumulus under stratocumulus layers (10–30%) and single-layer stratocumulus (0–10%) following in frequency of occurrence. A stable transition layer in the subcloud layer is commonly observed (92% of the soundings).. Cumulus cloud bases and stratocumulus cloud tops correlate very well with the top of the transition layer and the inversion base respectively. Drizzling stratocumulus layers are thicker (350–400 m) and have higher liquid water path (75–150 g m⁻²) than their non-drizzling counterparts (100–250 m and 30–75 g m⁻² respectively). The variance of the vertical air motion is maximum near the cloud base and is higher at night. The updraft mass flux is around 0.17 kg m⁻² s⁻¹, with 40–60% explained by coherent updraft structures. Despite a high frequency of stratocumulus clouds in the Azores, the MBL is almost never well mixed and is often cumulus-coupled.

1 1. INTRODUCTION

2

3 Marine stratocumulus clouds are ubiquitous over the eastern the subtropical oceans and
4 play a critical role in the boundary layer dynamics and the global climate (e.g., Klein and
5 Hartmann, 1993; Bony and Dufresne, 2005). These prevailing low-level cloud decks are a
6 key component in Earth's radiation budget (Randall et al., 1984; Ramanathan et al.,
7 1989). The radiative impact of marine boundary layer clouds depends on their
8 macroscopic properties (e.g., horizontal extent, thickness) and microscopic properties
9 (e.g., particle size distribution). Past studies have focused on the cloud macro-structure
10 properties of marine boundary layer clouds and their relationship to large-scale dynamics
11 and thermodynamic state using satellite observations and reanalysis products (e.g., Klein
12 and Hartmann, 1993; de Szoeke and Xie, 2008). Wood and Bretherton (2006), have
13 shown that approximately 80% of the variance in low cloud cover in regions dominated
14 by marine stratocumulus is explained using the estimated inversion strength. However,
15 appreciable complexity and challenges are found on smaller space and time scales,
16 including the cloud micro-scale (spatial scales of tens of meters and temporal scales of a
17 few minutes or less).

18 Previous field experiments focusing on marine stratocumulus clouds include the Atlantic
19 Stratocumulus Transition Experiment–ASTEX (Albrecht et al., 1995), the East Pacific
20 Investigation of Climate–EPIC (Bretherton et al., 2004), the Dynamics and chemistry of
21 marine stratocumulus–DYCOMS (Stevens et al., 2003), and the VAMOS Ocean-Cloud-
22 Atmosphere-Land Study Regional Experiment–VOCALS-REx (Wood et al., 2011).
23 These field studies advanced our knowledge of marine stratocumulus, providing

1 information on their boundary layer thermodynamic and cloud structure, as well as their
2 diurnal cycle. They have highlighted that stratocumulus clouds can form under a diverse
3 range of conditions, in both deep and shallow marine boundary layers (MBL), and under
4 a wide range of aerosol conditions. Furthermore, the radiative properties and propensity
5 for drizzle from marine stratocumulus clouds depend on several factors including
6 aerosols, liquid water path and dynamics.

7 The aforementioned field campaigns are characterized by intensive observation periods
8 limited in time from a couple of weeks to a month. Thus, previous studies have not been
9 carried out long enough to provide a useful climatology of key MBL and associated cloud
10 properties. The recent Clouds, Aerosol and Precipitation in the Marine Boundary Layer
11 (CAP-MBL) field campaign (www.arm.gov/sites/amf/grw/) that took place in the Azores
12 nicely filled that gap. As part of the campaign, the US Department of Energy
13 Atmospheric Radiation Measurements (ARM) Mobile Facility (AMF) was deployed on
14 Graciosa Island. This AMF deployment is unique compared to previous intensive field
15 campaigns. First, the AMF instrumentation is far more comprehensive and superior to
16 that available in previous ground-based field studies. Second, the campaign is 21 months
17 long and thus provides the opportunity to generate the long data set record required to
18 sample a variety of aerosol, cloud and large-scale environmental conditions. Finally, it is
19 the first marine stratocumulus field campaign with sophisticated cloud radars (profiling
20 and scanning) on a stable (island) platform that enables the use of the Doppler velocity
21 measurements. Thus, the AMF deployment in the Azores produced the most
22 comprehensive data set of MBL clouds to date.

1 In this study, we select a subset of the deployed AMF instruments to study the observed
2 MBL clouds in more detail. An objective scheme was first developed to identify their
3 occurrence across the entire data set, and to recognize some important subtypes (e.g.,
4 cumulus and stratocumulus), with the presence of precipitation also diagnosed (see
5 section 3). The variability and frequency of occurrence of the different cloud and
6 precipitation events is presented with emphasis on the various MBL cloud structures. A
7 further analysis of the MBL emphasizes the differentiation between cumulus and
8 stratocumulus regimes, as well as the presence of decoupling. A statistical analysis of
9 cloud structural and dynamical properties is performed, and related to the thermodynamic
10 profiles.

11

12 **2. OBSERVATIONS**

13

14 The CAP-MBL field campaign lasted 21 months (April 2009 to December 2010),
15 permitting the sampling of almost two full years of cloud and precipitation conditions in
16 the Azores. Although this location has been used in the past for the study of marine
17 stratocumulus clouds (ASTEX), a variety of cloud conditions were sampled which
18 include shallow cumulus, cumulus under stratocumulus, deeper convection and frontal
19 systems. The AMF, with its usual comprehensive array of aerosol, cloud, precipitation
20 and radiation sensors was deployed near the north shore of Graciosa Island (39.09°N,
21 28.03°W, 26 m above mean sea level). This location is upwind for the climatologically
22 prevailing wind conditions in the MBL and was selected to reduce the island effect. The
23 primary instruments used in this study to describe the cloud and precipitation conditions

1 are: a W-band (95-GHz) Doppler radar, a laser ceilometer, a two-channel microwave
2 radiometer and radiosondes (four per day). The instruments were placed within a few
3 meters of each other; thus, to the extent possible, their measurements describe the same
4 atmospheric column. The operational status of the three remote sensors is summarized in
5 Fig. 1, allowing gaps of up to one minute to be considered within normal operation.
6 Overall, the observations are fairly continuous with great overlap between the three
7 remote sensors, spatially as well as temporally.

8

9 **2.1 W-band Doppler radar**

10

11 A baseline instrument of the AMF is the W-band ARM Cloud Radar (WACR; Mead and
12 Widener, 2005), a 95-GHz vertically pointing Doppler radar. Millimeter wavelength
13 radars are ideally suited for the study of MBL clouds (e.g., Kollias et al., 2007a). Due to
14 its short wavelength (3.15 mm), it is sensitive enough to detect cloud droplets (-50 dBZ at
15 2 km), while attenuation is small in light to moderate drizzle conditions. Furthermore, it
16 uses a beam width narrow enough (0.19°) to provide high temporal and spatial
17 resolutions (respectively around 2 s and 43 m). Its primary measurement is the Doppler
18 spectrum, reporting the full distribution of the returned radar echo over the range of
19 sampled Doppler velocities (here $\pm 7.885 \text{ m s}^{-1}$, with a resolution near 6 cm s^{-1}). Thus,
20 detailed information about cloud microphysics and dynamics are inherent in the radar
21 measurements (e.g., Kollias et al., 2011a; Luke et al., 2010). The WACR also provides an
22 estimate of hydrometeor (i.e., cloud and drizzle) boundaries (see section 3.1 below), as it
23 is only sensitive to these atmospheric particles. However, some parts of non-precipitating

1 liquid clouds might be missed if the cloud droplets are not large enough, and heavy
2 precipitation strongly attenuates the signal affecting the cloud top measurements. For the
3 Azores deployment, the WACR began operating on the morning of 5 June 2009, and
4 operated until the end of the campaign. One major interruption occurred in September
5 2010, when the radar was down for almost 23 days, due to a hard disk problem.
6 Otherwise, the radar experienced six downtimes of more than an hour (including three
7 extending over about 1.5 day), and a few shorter, for a total of less than 10% of a month
8 (see Fig. 1, black bars). Note also that the radar used alternating co- (H-H) and cross-
9 polarized (H-V) operating modes through late 2009, after which it operated continuously
10 in co-polarized mode. The cross-polarized measurements are not used here, since MBL
11 clouds have spherical cloud and drizzle particles. Therefore, the time between profiles is
12 around 4 s for the earlier months, and 2 s for the latter. Nonetheless, given the horizontal
13 scales of the sampled clouds the results should not be affected by that change.

14

15 **2.2 Ceilometer**

16

17 Another baseline AMF instrument is a Vaisala ceilometer (CT25K model, upgraded in
18 mid-July 2010 to the CL31 model; Munkel et al., 2007), a near-infrared vertically
19 pointing lidar. It provides profiles of the atmospheric column, sensing aerosols and
20 hydrometeors mainly up to the liquid cloud base, as cloud droplets prevent in-cloud
21 measurements by extinguishing the laser signal. Nevertheless, the sharp increase and
22 subsequent decrease of the lidar backscatter at the level of the cloud base is very useful
23 for deriving the actual cloud base height, while still being able to profile drizzle and

1 aerosols particles under the cloud (e.g., O'Connor et al., 2005; Markowicz et al., 2008).
2 Although up to three liquid layer bases are reported in the ceilometer products, usually
3 only the first one is reliable. This is due to the quick depletion of the lidar signal strength
4 by the numerous cloud droplets, and it depends on the amount of liquid encountered in
5 lower cloud layers. The ceilometer's temporal resolution was around 15 s for this
6 deployment, which is slightly coarser than the WACR's. Here, it is assumed that each
7 reported base height is representative of the whole 15 s. The ceilometer range resolution
8 is 15 m. Thus, the analysis is done using the original WACR temporal grid, maintaining
9 the high sampling rate of the WACR. The ceilometer was deployed for the whole
10 duration of the campaign. It only experienced 12 downtimes lasting more than an hour
11 (including three covering more than a day), as well as a small number of shorter
12 interruptions (see the dark bars in Fig. 1).

13

14 **2.3 Microwave radiometer**

15

16 A standard Radiometrics 2-channel microwave radiometer (MWR) was also present
17 throughout the campaign. This instrument passively measures the amount of radiation
18 emitted by the atmosphere at two frequencies (23.8 and 31.4 GHz) to retrieve the amount
19 of integrated water in the atmospheric column overhead, separated into the vapor and
20 liquid phases (respectively the precipitable water vapor (PWV) and liquid water path
21 (LWP); e.g., Liljegren, 1994). Such information can help constrain retrievals from other
22 instruments, such as the WACR. The MWR time resolution is around 30 s, which is also
23 coarser than the WACR's. Nevertheless, as the MWR measurements actually come from

1 20-s signal dwells, it is reasonable to consider each retrieved quantity to be representative
2 of the whole 30 s. Therefore, these measurements are oversampled to match the high
3 temporal resolution of the WACR when required by the analysis. The root-mean-squared
4 accuracy of the LWP retrieval is around 20–25 g m⁻². As with the ceilometer, the MWR
5 was deployed for the whole campaign, and it worked continuously without much
6 interruption of data (see Fig. 1, light bars). However, the MWR experienced a processing
7 problem in the second summer, rendering the measurements reported from 11 July
8 through 9 August 2010 unreliable (not shown in Fig. 1 as measurements are available
9 nevertheless). Note also that the presence of water on the instrument's window
10 contaminates the measurements, rendering its retrievals unreliable. This happens anytime
11 precipitation reaches the ground.

12

13 **2.4 Radiosondes**

14

15 Regular radiosonde launches (every six hours) were performed throughout the
16 deployment to characterize the thermodynamic state of the atmosphere, as well as the
17 wind speed and direction. The radiosondes collect measurements every 2 s during their
18 ascent, providing a typical vertical resolution of 10 m in the troposphere (depending on
19 the conditions at the launch time). These measurements can only be interpolated to the
20 WACR time steps with limited confidence, due to the coarse temporal resolution of the
21 radiosondes. However, some statistics can still be determined around the balloon launch
22 times, since there are 20 months of data, comprising more than 2200 atmospheric

1 profiles, although no sondes were launched in the last third of October 2009, nor from 2
2 December 2009 through 12 January 2010 (see the numbers on top of Fig. 1).

3

4 **3. METHODOLOGY**

5

6 All instruments described in the previous section have certain skill for detecting the
7 presence of clouds in the overlaying atmospheric column. For instance, relative humidity
8 profiles taken by a radiosonde have been used in the past to provide estimates of cloud
9 layer locations (e.g., Wang and Rossow, 1995). But, their temporal resolution is too
10 coarse to form robust statistics of cloud occurrence, especially in the MBL, where clouds
11 are typically very thin. The MWR is sensitive to the presence of liquid in the column, and
12 measurements above its theoretical sensitivity ($30\text{--}50\text{ g m}^{-2}$) can be used to infer the
13 occurrence of liquid clouds. However, the MWR misses all ice clouds (mostly cirrus
14 clouds in the Azores), as their thermal emission is negligible at the frequencies sensed by
15 the MWR (Ulaby et al., 1981). Similarly, the ceilometer measurements are very sensitive
16 to the presence of cloud droplets, providing a good estimate of the base height of liquid
17 clouds; its backscatter profiles can be used to find ice cloud too (e.g., Liu et al., 2009).
18 Nevertheless, it still misses most high clouds, as its useful range stops near 7.5 km.
19 Finally, the WACR is sensitive to most hydrometeors, and profiles all clouds in the
20 troposphere, unless strong precipitation occurs and causes too much attenuation
21 (Lhermitte, 1990). However, it cannot easily differentiate precipitation from cloud
22 particles (so cannot be used to reliably provide cloud base estimates in drizzling
23 conditions), and lacks sensitivity to very thin liquid clouds (less than 100 m thick).

1 Here, a multi-instrument approach that utilizes synergistic measurements from all sensors
2 is used to describe the cloud and precipitation conditions during CAP-MBL. Due to the
3 focus on describing the vertical structure of clouds and precipitation, only the active
4 remote sensors (radar, lidar) measurements are used for the cloud and precipitation
5 occurrence statistics, while the MWR and the soundings are used as additional
6 classification variables. The approach is not new, the cloud radar and lidar are
7 complementary instruments often used to derive cloud and precipitation statistics (e.g.,
8 Intrieri et al., 2002; Bretherton et al., 2004; Kollias et al., 2007b, Illingworth et al., 2007).

9 Using the raw WACR measurements (radar reflectivity and Signal-to-Noise Ratio
10 (SNR)), the radar range gates that contain significant returns from atmospheric targets
11 (e.g., hydrometeors) are identified to develop the radar-detected hydrometeor mask. The
12 large number of WACR integrated radar pulses (~20,000 collected in 2-s signal dwell and
13 a WACR Pulse Repetition Frequency of 10 kHz) enables it to detect very low signal to
14 noise radar returns in the boundary layer (WACR sensitivity of -56 dBZ at 1 km). The
15 significant detection WACR hydrometeor mask is based on Clothiaux et al. (1995), and a
16 two-dimensional (time-height) filter is used to remove isolated radar pixels. The WACR-
17 derived hydrometeor mask is used to estimate the number of hydrometeor layers in the
18 atmospheric column and their corresponding boundaries. The WACR-derived
19 hydrometeor layer base is not necessarily the cloud base since the WACR cannot
20 differentiate between cloud and precipitation particles below the cloud base. Thus, the
21 radar-derived hydrometeor mask is combined with the ceilometer-generated time series
22 of cloud base heights. Although the ceilometer detects drizzle too, its measurements are
23 more sensitive to the numerous small liquid cloud droplets encountered by the laser at the

1 cloud base, and thus are systematically used to derive the liquid cloud base, at least for
2 the first cloud layer. As formerly observed (e.g., Comstock et al., 2004; Wood et al.,
3 2011), heavy drizzle often give false signals, by significantly lowering the ceilometer-
4 derived cloud base height. During heavy precipitation, the cloud identification will still
5 be reliable, but further analysis of MBL clouds would be compromised. Thus, the profiles
6 containing intense precipitation (defined below) are removed prior to subsequent
7 analysis.

8 The WACR/ceilometer detections agree very well in the MBL; however, the possibility
9 of underestimating the hydrometeor occurrence at high altitude should be considered
10 since the ceilometer is not capable of detecting high clouds and the radar sensitivity is
11 degraded. The WACR moments, the radar-derived hydrometeor mask and the ceilometer-
12 derived liquid cloud base are inputs to the cloud and precipitation type identification
13 scheme described in the following section.

14

15 **3.1 Cloud and precipitation type identification**

16

17 A WACR echo is classified as precipitation if it is detected below the ceilometer cloud
18 base height. The first category of precipitation is virga, defined as precipitation that does
19 not reach the lowest WACR range gate (i.e. no significant radar return at its lowest range
20 gate, around 170 m AGL; see Table 1a). In cases where the WACR echoes reach the
21 lowest range gate (here taken as a proxy for the surface), two more precipitation
22 categories are identified: light and intense. The separation between these two

1 precipitation types is based on a near-surface (200 m) radar reflectivity threshold of 0
2 dBZ. Anytime the WACR lowest gate echoes have a reflectivity above 0 dBZ, intense
3 precipitation is designated, regardless of the ceilometer cloud base height, since the
4 ceilometer measurements are significantly affected by the presence of water on its lens
5 cover. The use of a radar reflectivity threshold is justified given the absence of
6 disdrometer measurements in the Azores. Furthermore, the MBL clouds produce drizzle
7 echoes below 0 dBZ; thus, the intense category of precipitation is almost exclusively
8 related to deeper cloud systems (e.g., frontal precipitation). The distinction between virga
9 and light precipitation provides a qualitative indicator of the drizzle intensity and
10 indicates the portion of the subcloud layer that was affected by evaporation.

11 Using the WACR-derived hydrometeor mask and the ceilometer-derived cloud bases,
12 groups of connected pixels containing hydrometeors are identified. Each of these
13 hydrometeor clusters is individually analyzed on an hourly basis, with the hydrometeor
14 layer base (top) defined as the 5th (95th) percentiles of the hourly distribution of the cloud
15 cluster base (top). Based on their hourly-derived base and top height extrema and the
16 available ceilometer-derived cloud base height, several cloud types are identified (Table
17 1b, columns). The hourly clusters are first separated into 4 types based specifically on
18 these boundary definitions: 1) high cloud if the base is above 7 km; 2) middle cloud if the
19 base is above 3 km; 3) low cloud if the top is below 3 km; and 4) deep BL cloud if the
20 base is below 3 km, but the top is above 3 km. Note that the last category contains mostly
21 frontal clouds, such as nimbostratus and cumulonimbus. Since the focus of this study is
22 MBL clouds, emphasis is placed on low clouds, where the radar and lidar are most
23 sensitive, allowing for well defined cloud boundaries. As a result, low clouds are further

1 divided into three sub-types: broken, stratocumulus, and indeterminate. The temporal
2 duration of a hydrometeor cluster is used to differentiate broken cloud conditions
3 (shallow cumulus) from stratiform cloud conditions, while stratocumulus are also
4 required to have a narrow hourly cloud top height distribution (less than 100 m standard
5 deviation). Examples of stratiform and broken MBL cloud conditions as seen by the
6 WACR and MODIS are shown in Fig. 2. The remaining low cloud hourly clusters make
7 up the third sub-type (referred to as indeterminate hereafter). Each cloud type has an
8 expected precipitation type (last row of Table 1b), although others are also possible. Note
9 that the lidar measurements rarely reach high clouds, and thus no precipitation shaft is
10 expected. Note also that the cloud types are not all mutually exclusive, since clouds are
11 observed only in time and height, yet they are also evolving in the two horizontal
12 dimensions.

13 The cloud and precipitation identification scheme is applied each day when both the
14 WACR and ceilometer were operational, and statistics about cloud and precipitation
15 occurrences are computed on hourly and daily basis, with the daily results composited
16 together to form monthly statistics. Note that the hourly-derived boundaries extrema are
17 only used to identify the cloud types. Further analysis makes use of the full distribution of
18 the hourly cloud base and top heights to provide their statistics. Finally, the occurrences
19 of cumulus clouds under a stratocumulus cover are investigated. These represent the
20 WMO-defined low cloud type CL8, and are diagnosed on an hourly basis. When both
21 types are detected in any number of profiles within an hour, all profiles having cumulus
22 and/or stratocumulus clouds within that same hour are included in the Sc+Cu category.

23

1 3.2 Radiosonde analysis

2

3 Radiosonde data are not used directly in cloud identification, but are used to determine
4 the thermodynamic structure of the lower atmosphere during certain cloud conditions.
5 For instance, the inversion often associated with the top of the MBL is easily detected in
6 sounding profiles. A temperature increase with height somewhere between 500 m (to
7 avoid surface effects) and 3 km (to remain in the MBL) denotes the presence of an
8 inversion. The level of maximum increase indicates the inversion layer location, and it
9 includes all levels around it still characterized by an increase. Since wetting affects the
10 temperature measurements above clouds (Caldwell et al., 2005), a loose criterion on the
11 water vapor mixing ratio (r) was added by requiring its decrease with height.

12 Many studies have also mentioned the presence of a transition layer in the MBL, which
13 separates a surface mixed layer from the cloud containing layer aloft (Augstein et al.,
14 1974; Garstang and Betts, 1974; Yin and Albrecht, 2000). It is mainly characterized by a
15 sharp decrease of moisture with height, accompanied by a slight increase in temperature.
16 It indicates the presence of decoupling conditions that can lead to a cut-off of the upper
17 part of the MBL from its moisture supply, thus controlling low-level cloudiness. Cumulus
18 clouds often form near its top, as the surface lifting condensation level often falls within
19 the transition layer (Yin and Albrecht, 2000). Following Yin and Albrecht (2000), the
20 presence of a transition layer will be investigated using their parameter μ , which
21 combines the potential temperature θ and mixing ratio r gradients with respect to the
22 pressure p in the following way:

$$\mu = - \left(\frac{\partial \theta}{\partial p} - \frac{0.608 \theta}{1 + 0.608 r} \frac{\partial r}{\partial p} \right).$$

1
2 Its mean value is computed using all levels below the inversion. Then, if the maximum
3 value of μ in those levels is positive and greater than 1.3 times the mean (based on Yin
4 and Albrecht, 2000), a transition layer is present. The transition layer includes all levels
5 around the μ maximum that satisfy this criterion.

6 As the detection of these two layers depends on the derivative of the measured variables,
7 a 1-2-1 smoother is applied prior to any analysis. This step removes most of the small-
8 scale variability that might be caused by sampling errors (although the data were already
9 smoothed by the radiosonde software itself), and provides smooth local gradients. Also,
10 when averaging various profiles together, a layer-by-layer procedure is used to preserve
11 the character of the transition and inversion layers (based on Augstein et al. (1974) and
12 Yin and Albrecht (2000)). For each sounding, five layers are defined: below the transition
13 base, the transition layer, from the transition top to the inversion base, the inversion layer,
14 and above the inversion top (up to 3 km). Each layer is averaged separately using a
15 relative height coordinate (from 0 to 1). The averaged sounding is then obtained by
16 combining the five resulting averaged layers, using the averaged base and top heights of
17 the layers to get the height coordinate.

18 The lower tropospheric stability (LTS) is also used in this study. Based on Klein and
19 Hartmann (1993), it is defined as the difference in potential temperature between 700 mb
20 and the surface. Finally, any interpolated (or averaged) wind direction is obtained from
21 the two interpolated (or averaged) components of the wind vector.

22

1 3.3 Turbulence and mass flux measurements

2

3 During non-precipitating cloud conditions, the WACR Doppler velocity measurements
4 are used to derive turbulence statistics in low-level stratiform cloud conditions. This is
5 based on the assumption that liquid cloud particles have negligible terminal velocity and
6 inertia, and thus act as tracers of the vertical air motion (e.g., Kollias et al., 2001). Only
7 stratocumulus periods without drizzle detected under the ceilometer base are considered
8 in these statistics, in order to remove most bias caused by the larger precipitating
9 particles. The WACR Doppler velocity measurements are used to estimate the hourly
10 estimates of the mean, variance and skewness of the vertical air motion. Using the
11 vertical air motion measurements, mass flux statistics are also estimated during non-
12 precipitating stratocumulus conditions to reduce any correlations between drop fall
13 velocities and WACR Doppler measurements. Although Kollias et al. (2011b) showed
14 that drizzle drops are ubiquitous in marine stratocumulus clouds, their impact on the
15 velocity moments remains negligible in non-drizzling parts.

16 Using the high-resolution in-cloud vertical velocity measurements, the mass flux profiles
17 are derived using two conditional sampling strategies (based on Kollias and Albrecht,
18 2000). They are both based on the WACR perturbed velocities, which are obtained by
19 removing the hourly mean from the velocity measurements. The first method (a classic
20 direct sampling) simply uses the sign of these perturbed velocities to determine the
21 presence of updraft and downdraft regions. The second method (the coherent sampling)
22 refines this by using the cloud's coherent structures only. Those structures are pockets of
23 clouds that move together on average. Coherent structures must be observed in both

1 dimensions: the perturbed vertical velocity must conserve its sign for three or more
 2 successive profiles (time dimension, which relates to the horizontal dimension), and over
 3 at least four successive gates (i.e., about 170 m in the vertical dimension). Both methods
 4 directly retrieve the fractional updraft area (σ) and the updraft and downdraft velocities
 5 (w_u, w_d), with the second one providing the contribution from the coherent structures. The
 6 convective mass flux (M_c) can then be computed from the following: $M_c = \rho \sigma (1 - \sigma) (w_u - w_d)$,
 7 where ρ is the air density.

8 The mass flux profiles are also computed using the turbulence statistics as proposed by
 9 Randall et al. (1992). This method relates σ and M_c to turbulence statistics. It uses a “top
 10 hat” representation of the updrafts and downdrafts properties to express σ , w_u , and w_d as
 11 functions of the first three moments of the vertical velocity (mean \bar{w} , variance S_w^2 , and
 12 skewness S_w):

$$13 \quad \sigma = \frac{1}{2} - \frac{S_w}{2\sqrt{4 + S_w^2}},$$

$$14 \quad w_u = \bar{w} + \frac{\sqrt{w'^2}}{2} \sqrt{4 + S_w^2} + S_w,$$

$$15 \quad w_d = \bar{w} - \frac{\sqrt{w'^2}}{2} \sqrt{4 + S_w^2} - S_w.$$

16 Then, the relationship for the convective mass flux depends only on the variance and
 17 skewness of the vertical velocity:

$$18 \quad M_c = \frac{\rho \sqrt{w'^2}}{\sqrt{4 + S_w^2}},$$

1 (see Randall et al. (1992) for the complete derivation of the equations). In the following
2 results, the mass flux values are normalized by ρ . The application of the Randall et al.
3 (1992) approach to estimate the fractional area of the updrafts and the updraft mass flux
4 and its comparison with the direct and coherent methods are used as a qualitative
5 indicator of how close to the top-hat representation of up- and downdrafts the observed
6 vertical air motion is. Furthermore, it is an indicator of how well high-order closure
7 models can be used to determine the area and mass flux of updrafts.

8

9 **4. RESULTS**

10

11 **4.1 Cloud and liquid precipitation occurrence**

12

13 Using the radar-lidar synergistic observations, the monthly fraction of time hydrometeors
14 were detected in the atmospheric column is shown in Fig. 3a. A weak seasonal cycle is
15 observed with minimum (60–70%) during the summer and early fall and maximum
16 (80%) during the winter and spring season. Liquid precipitation is detected almost 50%
17 of the time that we have hydrometeors in the atmospheric column and exhibits a similar
18 weak seasonal cycle. A breakdown of the observed cloud occurrence into the four main
19 cloud types (described in section 3.1) is shown in Fig. 3b. Note that the sum of these
20 cloud type occurrences is likely greater than (rather than equal to) the overall cloud
21 occurrences shown in Fig. 3a, since more than one cloud type can be present in the
22 atmospheric column at the same time. Low-level clouds are the dominant observed cloud

1 type, with 40–60% occurrence maximizing in the summer and fall seasons. The seasonal
2 cycle of low cloud occurrence anti-correlates with the observed seasonal cycle of all the
3 other cloud types which peaks during the winter and spring seasons (Fig. 3b), consistent
4 with the presence of the subtropical high-pressure system during the summer and fall
5 seasons that favors MBL cloud occurrence through the development of low tropospheric
6 stability and moisture trapping in the low levels. This system is strongest in summertime,
7 when mid-latitude storm tracks are at their most poleward, and with its center closer to
8 the site (Hasanean, 2004), explaining the seasonal cycle observed, as proposed by Norris
9 and Klein (2000). A local minimum in the low clouds occurrence is noticeable in the
10 early fall of 2009 (a corresponding 2010 event is unconfirmed due to the radar failure in
11 September 2010). This divergence could be a simple manifestation of inter-annual
12 variability, experiencing more mid-latitude systems than normal. A longer time series is
13 needed to verify this feature.

14 Additional insights on the seasonal cycle of low-level clouds are provided through their
15 breakdown into different subtypes (see Fig. 3c). Shallow cumulus clouds are the most
16 frequently observed MBL cloud type with a monthly occurrence of 20% and weak
17 month-to-month variability during the summer. Monthly increases in Sc+Cu coverage
18 appear to compensate for decreases in the Cu cloud fraction. Indeed, this MBL cloud
19 structure is also frequently observed, with maximum occurrences during the summer
20 months. In fact, they follow a similar annual cycle as the single-layer stratocumulus
21 clouds, which are the least observed MBL cloud type, especially during the winter and
22 spring months. Nevertheless, the dataset is only long enough to derive an anecdotal
23 seasonal climatology, as revealed by the differences between months in the first and

1 second years. As for the indeterminate category, it has typical occurrences around 10%
2 with small intraseasonal variability. Such low values probably come from the
3 intermediate state of this type, acting as a transition between the other clouds based in the
4 MBL (i.e., low and deep BL clouds).

5 The LTS has often been linked to the presence of low clouds. For instance, Zhang et al.
6 (2010) provided coarse threshold values of LTS, less than 14K and greater than 19K, for
7 small and large low-cloud fractions, respectively. These values correlate well with the
8 cumulus and stratocumulus covers (see Fig. 3e). In fact, increases in LTS are usually
9 associated with increases in stratocumulus coverage. Moreover, most values are close to,
10 or above, the 14K threshold, allowing cumulus clouds to form. This emphasizes the
11 greater stability (mean of 17K) found in the Azores, compared to the eastern equatorial
12 Pacific (13K, see Yin and Albrecht, 2000).

13 Fig. 3a demonstrates the propensity of marine clouds to produce precipitation. However,
14 it often completely evaporates before reaching the surface, as illustrated by the separation
15 into the three types considered (virga, light, and intense) in Fig. 3d. Intense precipitation
16 occurs mostly during fall and winter, weakly following the presence of deep BL clouds,
17 suggesting that it is primarily associated with stronger and deeper systems. Other
18 precipitation categories display no obvious annual variability.

19

20 **4.2 Stratocumulus and cumulus cloud base height statistics**

21

1 According to Table 1b, stratocumulus and cumulus clouds are separated based on their
2 horizontal extent. Furthermore, their cloud base height statistics are different and this
3 improves the robustness of the radar-lidar based classification algorithm. The
4 distributions of their hourly-averaged cloud base heights are compared in Fig. 4a. Only
5 hourly periods with a cloud fraction greater than 10% for the given type are included in
6 the analysis. In addition, any hourly period with intense precipitation is also excluded to
7 avoid possible contamination of the ceilometer cloud base. Although considerable
8 variability in the cloud base occurrences of these two cloud types is observed, a
9 separation is clearly visible between the two distributions, with cumulus clouds forming
10 lower than stratocumulus clouds. This is consistent with the frequently observed cumulus
11 under stratocumulus MBL cloud structure in the Azores. Yet, some stratocumulus bases
12 have been detected at very low altitudes (below 500 m, below most cumulus). Such low-
13 based stratocumulus clouds have been sampled during ASTEX (de Roode and
14 Duijnkerke, 1997); however, fog-like conditions could have contaminated the statistics.

15 The hourly-averaged stratocumulus cloud top height and cumulus cloud base height are
16 compared with the MBL inversion base and the transition layer top respectively (Fig. 4b).
17 The MBL inversion base and transition layer top are estimated from the radiosondes. The
18 cloud boundary heights used in the comparison with the radiosondes are one-hour
19 averages centered on the sounding launch time. In addition, a minimum of 10% cloud
20 fractional coverage is required, and the absence of intense precipitation. The results are
21 again in reasonable agreement with the expectations: both distributions are peaking near a
22 zero difference, although the cumulus cloud base exhibits higher variability around the
23 transition layer top. The broader distribution of cumulus cloud base heights around the

1 transition layer top height can be partially explained by their intermittent character and
2 their role in maintaining the transition layer in the first place (Stevens, 2007) and the
3 difficulty in retrieving the hourly-averaged cloud base especially in shear conditions.
4 Furthermore, part of the variability might be caused by the challenge of correctly
5 detecting the transition layer in noisy soundings and from cumulus clouds linked to other
6 clouds (i.e., breaking deep BL, stratocumulus or indeterminate clouds).

7 The double-peak cloud base height structure observed for the stratocumulus clouds is
8 explained by their seasonal cycle (Fig. 5a). The lower peak (around 1100 m) results from
9 summer cases, while the higher peak (around 1600 m) results from the transition periods
10 (spring and fall, mainly May and September). The winter season did not experience much
11 stratocumulus coverage (as noticed in Fig. 3c), and thus does not contribute much. This
12 seasonal dependence could be linked to the dominant air mass, which in turn is
13 influenced by the strength of the high-pressure system. The agreement between the
14 stratocumulus tops and the inversion base is still visible after averaging them monthly,
15 except in winter when the stratocumulus clouds are less frequent (Fig. 5a). Interestingly,
16 the averaged stratocumulus top is sometimes within the inversion layer. This agrees well
17 with recent in situ observations (e.g., Carman et al, 2012), although the measurements
18 have a great variability (not depicted here) due to intra-seasonal variations and various air
19 mass intrusions. Another noticeable finding is the very frequent occurrence (higher than
20 80%) of inversion and transition layers in the MBL throughout the field campaign (Fig.
21 5b). The occurrence is based on the monthly fraction of soundings with inversion and/or
22 transition layers. The persistence of transition layers indicates the lack of well-mixed
23 conditions in the subcloud layer.

1

2 **4.2.1 MBL variability during single and multilayer cloud conditions**

3

4 A detailed analysis of the MBL variability during stratocumulus and stratocumulus over
5 cumulus conditions and their corresponding MBL thermodynamic structure is presented
6 here. Since a vertical stratification of the MBL influences these low clouds' development,
7 the MBL thermodynamic structure is first investigated using the soundings directly,
8 without classifying them by cloud type (see Fig. 5b). Inversion-topped MBL were
9 encountered by 95% of the soundings. Interestingly, the remaining 5% of the soundings,
10 which are inversion-free, occurred mostly in wintertime, the season when deep systems
11 are more frequently observed. This also supports the strong influence of the nearby high-
12 pressure system, which would sustain the inversion cap through the divergence it creates.
13 Similarly, 92% of the soundings presented a transition layer signature. However, this
14 fraction is roughly the same for all studied months, showing no clear preference to any
15 season. This is consistent with the constant coverage of cumulus clouds throughout the
16 campaign, which help create and maintain this MBL structure (Stevens, 2007).

17 The proportions of transition and inversion layers found in soundings are much larger
18 than observed over the eastern equatorial Pacific (Yin and Albrecht, 2000). It is
19 reasonable to hypothesize that significantly strong mixing in the layer above the
20 transition is required to support a clear temperature jump at its base. Radiative cooling
21 associated with extensive clouds in the upper MBL may provide such mixing. In purely
22 trade cumulus BL, this mixing is less efficient and the transition layer is less well defined.

1 Interestingly, the transition layer height closely follows the inversion base height
2 annually (see Fig. 5a), which further supports this hypothesis.

3 The MBL thermodynamic structure is also analyzed using its cloud structure. Every hour
4 of the day, the time fraction of multilayer low clouds is recorded along with the standard
5 deviation of the ceilometer first cloud base. If multilayer conditions exist for more than
6 10% of the hour and the cloud base standard deviation is larger than 300 m (depicting
7 broken clouds under a stratiform layer), then the hour is classified as multilayer cloud
8 condition. On the other hand, if only a single cloud layer is detected within the hour and
9 the cloud base standard deviation is less than 100 m (ensuring a single level), then the
10 hour is classified as single layer cloud condition. Using the number of hours every month
11 classified as single or multilayer cloud conditions, their diurnal and seasonal cycle can be
12 estimated (Fig. 6). The observations suggest the presence of a weak diurnal cycle with
13 increased single-layer occurrences during daytime, and the opposite for multilayer
14 conditions. Although this seems counter-intuitive from a diurnal decoupling view, it is
15 supported by the near-constant decoupled state of the MBL (see Fig. 5b), allowing
16 cumulus to be omnipresent, while stratocumulus tend to fill in preferentially during
17 nighttime. On the other hand, the MBL does show more multi-layer cases in the
18 wintertime and more single-layer clouds in the summertime, with associated transitions in
19 the spring and fall seasons. This result is consistent with a weaker high-pressure system
20 in winter, allowing for a weaker and higher (see Fig. 5a) inversion, providing more
21 vertical extent to form multiple clouds.

22 The soundings collected within an hour of single and multilayer cloud conditions are
23 further analyzed to identify the main feature of their corresponding thermodynamic

1 structure in the MBL. Each sounding is first analyzed separately to detect the height of
2 the inversion and transition layers (if present). The analysis indicated that the vast
3 majority of the analyzed soundings that correspond to both single and multilayer cloud
4 conditions show a transition layer (as seen in Fig. 5b). The soundings that did not have a
5 detectable transition layer in the MBL were shallow (inversion height below 1 km),
6 which might have prevented the complete formation of a transition layer. This concurs
7 with previous studies (Albrecht et al., 1995; Wood and Bretherton, 2004) suggesting that
8 the atmospheric BL must be deeper than about 700 m to have a decoupled structure.

9 The single cloud layer soundings are separated in two subsets, according to the
10 thermodynamic layer linked to the cloud layer: the inversion (SLa) or the transition
11 (SLb). A third category of soundings corresponds to multi-layer cloud conditions (ML).
12 Although the cloud type is not directly used in this classification, each group corresponds
13 to a different MBL situation: stratocumulus (SLa), cumulus (SLb), and stratocumulus
14 with cumulus underneath (ML). Using all the soundings with a transition layer,
15 composited profiles were obtained for each group following the layer-by-layer averaging
16 method described in section 3.2 (see Fig. 7). The SLa cases have a lower averaged
17 inversion height, reminiscent of the difficulty to fully decouple shallow MBL. They also
18 have the strongest potential temperature and mixing ratio jumps through the inversion
19 layer associated with the weakest jumps at the transition layer, supporting only the
20 stratocumulus cloud. Comparatively, both layers show strong jumps for the SLb cases. A
21 strong inversion in both types of single layer cases is consistent with their tendency to
22 occur during summer, when the high-pressure system is stronger.

1 The averaged profiles of potential temperature and mixing ratio exhibit a gradual
2 transition from the stratocumulus (SLa) to stratocumulus-with-cumulus (ML) to cumulus
3 (SLb) cloud regimes, supporting the usual picture of the transition from mid-latitude to
4 tropical MBL often experienced in the Azores (de Roode and Duynkerke, 1997). The
5 profiles with the lowest relative humidity correspond to cloud conditions associated with
6 the transition layer only (SLb group), consistent with the broken nature of cumulus
7 clouds. Multi-layer cloud conditions show higher wind magnitudes on average. However,
8 there is a great variability associated with the wind measurements, partly due to seasonal
9 differences (not shown). The wind direction averaged profiles are very similar above the
10 base of the transition layer; however, an easterly wind at the surface seems to be linked
11 with single cloud layer detections near the inversion. Although not shown here, this
12 change in direction in the SLa group happens in the summer, while fall cases are more
13 unidirectional. Also, winter and spring single-layer cases tend to have a greater southern
14 component. However, due to the wide range of variability in the data, more cases are
15 needed to verify the existence (or lack of) of a preferred wind speed and direction (or
16 synoptic situation) for each MBL structure through the seasons.

17

18 **4.3 Stratocumulus clouds**

19

20 **4.3.1. Macroscopic properties and thermodynamic structure**

21

1 Using the hours with single layer stratocumulus conditions, thirty-five days where
2 stratocumulus clouds persist through most of the day are selected for additional analysis.
3 Most of the selected days occurred in early summer (June–July) or late fall (October–
4 November). During the summer period, stratocumulus clouds have lower cloud base
5 heights compared to the late fall (causing the bimodal structure in Fig. 8a, as previously
6 noticed in Figs. 4 and 5a using all stratocumulus clouds). Distinct difference in the
7 distribution of cloud thickness is observed during drizzling (excluding intense
8 precipitation) and non-drizzling conditions. The distribution of cloud thicknesses for
9 periods with a drizzle shaft peaks around 250–300 m, while the distribution of cloud
10 thicknesses for periods without virga peaks at 150 m (Fig. 8b). On the contrary, there is
11 no clear difference in the distributions of cloud bases using the same separation (see Fig.
12 8a). The peak below 200 m for the cases “without drizzle” comes mostly from periods
13 when the ceilometer measurements are compromised by heavy precipitation, as they
14 correspond to the tail of larger depths seen in Fig. 8b.

15 Another way to demonstrate the difference in cloud thickness during drizzling and non-
16 drizzling periods is through their corresponding distributions of LWP (see Fig. 8c).
17 Although small amounts of liquid water are possible in drizzling and non-drizzling
18 stratocumulus clouds, LWP greater than 75–100 g m⁻² are sufficient to produce drizzling
19 conditions. This result compares well with previous studies conducted in various
20 stratocumulus decks (e.g., Wood, 2005; Zuidema et al., 2005; Serpetzoglou et al., 2008;
21 Kubar et al., 2009). Moreover, the non-drizzling distribution peaks around 30 g m⁻²,
22 which is near the theoretical accuracy of the deployed MWR. Also, as before, the tail of

1 greater LWP visible for the non-drizzling profiles is associated with the deeper
2 stratocumulus clouds with bases affected by precipitation.

3 The soundings recorded during the selected thirty-five days are used to describe the
4 inversion and transition layer characteristics. As expected, all the recorded soundings
5 indicate the presence of an inversion layer near the stratocumulus cloud top. Due to their
6 small number (141) and the difficulty to properly define the associated drizzling
7 character, no separation was performed. The depth of the inversion layer shows a strong
8 peak just below 200 m (see Fig. 8d). This is much deeper than most observations (e.g.,
9 Carman et al., 2012) and simulations (e.g., Stevens et al., 1999). Nevertheless, this
10 derived quantity is likely influenced by the smoothing of the data by the sounding
11 software, as well as by wetting, which would have mainly caused an overestimate of the
12 layer top (see Caldwell et al., 1995).

13 The full distributions of the jumps in equivalent potential temperature ($\Delta\theta_e$) and water
14 vapor mixing ratio (Δr) are given in Fig. 7e. As observed in various stratocumulus
15 studies, $\Delta\theta_e$ is often negative. Although this situation can still satisfy the stability
16 criterion (Kuo and Schubert, 1988; MacVean and Mason, 1990) since Δr is usually also
17 negative, most values fall within the range generally accepted for the criterion, and only a
18 few soundings are clearly stable. Such persistence under unstable conditions has been
19 observed in other studies (e.g., Faloona et al., 2005; Carman et al., 2012). Yamaguchi and
20 Randall (2008) explain this behavior by the weakness of the feedback in stratocumulus.

21 Based on the methodology devised by Yin and Albrecht (2000) for the East Pacific (as
22 described in section 3.2), the presence of a transition layer was also diagnosed for most of

1 the persisting stratocumulus soundings, as the threshold value was usually exceeded (see
2 Fig. 8f). This suggests that the stratocumulus layer is decoupled from the surface.

3

4 **4.3.2 Diurnal cycle**

5

6 Using the hourly-derived statistics from the thirty-five selected days, a composite daily
7 cycle is derived for the occurrence and boundaries of the stratocumulus clouds and their
8 associated drizzle, using 3-hour bins (Fig. 9). As expected, the cloud fraction is very high
9 (>80%) throughout the day. The maximum values of cloud fraction are found during
10 nighttime, with a gradual decrease of coverage occurring in the morning hours, followed
11 by an increase after sunset, as in other marine decks (e.g., Ghate et al., 2009). The marine
12 stratocumulus clouds observed in the Azores are usually precipitating (70% of the time),
13 and the small decrease in cloud fractional coverage during daytime is also associated with
14 a reduced drizzling fraction reaching ground. In fact, while virga is constantly detected in
15 45% of an average stratocumulus, light precipitation has a marked decreased occurrence
16 during the day. As for intense precipitation, it rarely occurs in a stratocumulus (less than
17 5%), and it is mostly around sunset and sunrise. Note that the following panels of Fig. 9
18 show pseudo-daily cycles, as each value is the average weighted by the hourly fractions.
19 As such, periods from various cases are mixed together, and the resulting cycle should be
20 taken with a grain of salt, especially for the measurements affected by the seasons (e.g.,
21 boundaries heights).

1 Shallow MBL are needed during nighttime to observe non-drizzling conditions, as
2 indicated by the lower cloud boundaries, while the development of drizzle during daytime
3 does not depend on the MBL depth (Fig. 9b). Light drizzle periods correspond to thicker
4 cloud decks (450–550 m compared to 200–270 m) and higher LWP values (140–200 g m⁻²
5 to 30–60 g m⁻²). Interestingly, virga periods have similar cloud depths (around 300 m)
6 as the non-drizzling periods, but constantly show larger LWP values (70–100 g m⁻²).
7 Furthermore, only the LWP of virga periods have a distinctive daily cycle, with a
8 pronounced increase near sunset. A similar cycle is observed in the cloud depth of the
9 light drizzle periods, following its stratocumulus coverage (Fig. 9c-d). Note that the
10 variability between the cases remains important, creating some overlap.

11

12 **4.3.3 Vertical air motion statistics**

13

14 Vertical air motions play an important role in the evolution of stratocumulus. Considering
15 only the time periods without a drizzle shaft in the 35 selected cases, hourly vertical air
16 motion statistics are derived (section 3.3). Hours with less than 15% non-drizzling
17 coverage are discarded from the following analysis. In the analysis, positive velocities
18 indicate updrafts. Thus, negative skewness of the hourly distribution of vertical air
19 motion indicates the presence of a few strong narrow downdrafts compensated by many
20 weak broader updrafts. Daytime and nighttime composites of the vertical air motion
21 statistics are constructed to highlight differences between day (11:00–17:00 UTC) and
22 night (23:00–05:00 UTC) time periods. Time periods close to local sunrise or sunset are
23 discarded from this type of analysis to ensure a clear separation between the two periods.

1 The vertical air motion variance profiles peak at the cloud base (Fig. 10a). As noted in
2 previous studies of the MBL (e.g., Nicholls, 1989; Hignett, 1991; Lothon et al., 2005;
3 Guo et al., 2008; Ghate et al., 2010), it indicates a maximum of turbulent kinetic energy
4 near the middle of the MBL since our measurements cover the top part of the MBL
5 occupied with cloud. Higher variance is observed during nighttime, as observed by
6 Hignett (1991), and is consistent with turbulence driven by cloud-top radiative cooling.
7 This excess turbulent energy is responsible for the thickening of the stratocumulus deck,
8 as well as its higher cloud fraction and stronger drizzle presence. The nighttime skewness
9 profile of the vertical air motion is negative throughout the cloud layer (Fig. 10c). This is
10 consistent with cloud-top radiative cooling as the driving mechanism and most nocturnal
11 in situ observations (e.g., Kollias and Albrecht, 2000, Guo et al., 2008). During daytime
12 however, skewness values are closer to neutral in the lower two thirds. Near the cloud
13 top, both periods show a similar behavior, strong negative values, suggesting cloud-top
14 driven turbulence.

15 The diurnal evolution of the vertical air motion variance and skewness in the
16 stratocumulus layer is shown in Fig. 10b,d using 3-hour bins. The vertical air motion
17 variance maximum is still clearly at night in the bottom half of the cloud. The periods
18 exhibit the highest variance values in the lower part of the cloud: 21:00–24:00 UTC and
19 03:00–09:00 UTC. Minimum vertical air motion variance in the lower part of the cloud is
20 observed during the 12:00–18:00 UTC period. Close to the cloud top, the variance
21 appears consistently low through the day. The diurnal cycle of the vertical air motion
22 skewness better captures the role of cloud-top radiative cooling as a source of turbulence
23 during nighttime. Positive values are also observed, but mostly in the top half during

1 daytime, especially around noon when positive values appear to take over the whole
2 cloud, consistent with surface-driven turbulence.

3

4 **4.3.4 Updraft mass flux**

5

6 The in-cloud vertical air motions support a significant portion of the turbulent transport of
7 heat and moisture in the cloud layer. The turbulence transport is often organized in
8 temporally-spatially coherent updraft and downdraft structure. Here, the vertical air
9 motion measurements are separated into nighttime and daytime periods and the analysis
10 described in section 3.3 is applied to estimate the mean updraft and mean downdraft
11 velocity profiles, the updraft area profile and the updraft mass flux profile. The resulting
12 in-cloud profiles are shown in Fig. 11, using the three possible methods (direct, coherent
13 and statistical). First, note that the statistical technique gives generally the same profiles
14 as the direct sampling, despite a small overestimate of the magnitudes, as found in LES
15 models (Randall et al., 1992) and continental stratocumulus (Kollias and Albrecht, 2000).

16 The mean amplitudes of velocity in updrafts and downdrafts are very similar. This is
17 linked to the cloud separating into two halves (one going up, the other going down) on
18 average throughout its depth, which compares well with continental stratocumulus clouds
19 (e.g., Kollias and Albrecht, 2000; Ghate et al., 2010), and other marine cases (e.g.,
20 Nicholls, 1989; de Laat and Duynkerke, 1998). However, coherent structures are
21 responsible only for 40–60% of the total mass flux. The contribution of coherent
22 structures to the turbulent transport is maximized at night near the middle of the cloud.

1 The mean velocity of coherent structures is also stronger, as expected. Nevertheless, their
2 contribution to the mass flux is still limited, especially during daytime. As observed in
3 the majority of stratocumulus decks, the mass flux is greater during nighttime, and in the
4 bottom half of the cloud, when and where the turbulence is stronger. It is also linked to
5 the mean velocities being maximized near the cloud base ($\sim 0.5 \text{ m s}^{-1}$), decreasing with
6 height.

7 A similar analysis performed at the cloud base of cumulus gives comparable values,
8 although the night and day results are closer. The main differences are stronger mean
9 updraft and downdraft velocities, and a weaker contribution from nighttime coherent
10 structures. A more detailed analysis of the shallow cumulus clouds' dynamics in the
11 Azores can be found in Ghate et al. (2011).

12

13 **5. SUMMARY**

14

15 The CAP-MBL campaign led to the collection of an extensive and well documented,
16 ground-based dataset of MBL clouds. Here, the frequency of occurrence of different
17 cloud and precipitation types, along with their macroscopic properties (e.g., cloud
18 boundaries) and MBL structure are presented. Several remote sensors are used to develop
19 statistics of occurrence of various cloud and precipitation types. Clouds occur frequently
20 throughout the 19-month period that was analyzed (June 2009–December 2010), with a
21 maximum (80%) during the winter-spring months and a minimum (60–65%) during the
22 summer months. Precipitation occurrence is also very high (30–40%), but precipitation

1 only reaches the ground less than 15% of the time. Most intense precipitation events
2 correlate well with the occurrence of non-MBL clouds linking them to mid-latitude
3 cyclones during the winter and spring months.

4 A predominance of MBL clouds was observed all year long, while higher clouds show
5 enhanced occurrences in winter. Moreover, cumulus clouds are present during all
6 seasons, while stratocumulus clouds occur preferably during the transition periods. These
7 two types often occur together, with each type being tied to a distinct thermodynamic
8 layer (the cumulus to the transition layer, and the stratocumulus to the inversion layer).
9 The strength of the subtropical high-pressure system influences the height (and presence)
10 of the inversion, thus regulating the height of the stratocumulus layer, as well as the
11 possibility to create two cloud layers in the MBL. In fact, on average, a stronger θ
12 increase, a greater LTS value, and a lower inversion base tend to accompany a greater
13 surface pressure in the Azores (a proxy for the strength of the subtropical anticyclone). In
14 turn, although not shown here, a higher pressure also seems more favorable for a
15 stratocumulus formation alone, while the cumulus clouds would form underneath at
16 lower surface pressure.

17 Analysis of the sounding profiles demonstrates the near omnipresence of decoupling in
18 the Azores MBL, a new finding that is only made possible by the long measurements
19 made during the campaign. Cloud layers do not always reveal this decoupling, presenting
20 only one layer in the observations. A two-part explanation can be hypothesized. First, a
21 strong transition layer could prevent moisture from reaching the upper cloud layer.
22 Second, a transition layer too weak might be unable to prevent the vertical development
23 of cumulus clouds that would then fuse with the stratocumulus layer.

1 Thirty-five days characterized by the presence of persistent single-layer stratocumulus
2 clouds were selected to gain further insights on their diurnal cycle, their macroscopic
3 properties (LWP, cloud boundaries) and dynamics. The minimum cloud coverage is
4 observed in the afternoon. This is consistent with the findings of other studies using
5 ground-based and satellite observations and models (e.g., Rozendaal et al., 1995; Abel et
6 al., 2010). Although the fractions found here are greater (remaining above 80%), this is
7 probably a bias due to the selection of persisting stratocumulus layers. Diurnal clearing is
8 accompanied by a thinning of the cloud layer, and a decrease in ground precipitation
9 coverage and LWP. Again, this is consistent with other stratocumulus studies, such as
10 those performed in the South-East Pacific (e.g., Wood et al., 2002; Abel et al., 2010).
11 Furthermore, it was observed that stratocumulus is most likely to drizzle if the cloud
12 depth exceeds 250 m and the LWP is above 60 g m^{-2} . Local maxima of ground
13 precipitation coverage occur around sunrise and sunset.

14 We find that stratocumulus clouds are more turbulent during nighttime. Throughout the
15 day, the turbulence maximized in the bottom half of the cloud, except around sunrise and
16 after sunset when it extended through higher levels. Profiles of skewness from the
17 velocity time series are consistent with cloud-top radiative cooling during nighttime, and
18 surface heating around noon, as reported in many other stratocumulus clouds (e.g.,
19 Kollias and Albrecht, 2000). Mass flux is greater at night, with the updrafts covering
20 about half of the cloud, in accordance with observations in other decks and current
21 theories (e.g., Nicholls, 1989; de Laat and Duynkerke, 1998; Kollias and Albrecht, 2000).
22 However, coherent updraft structures contribute 40 to 60% of the total updraft mass flux.

1 Higher contributions (70 to 75%) have been observed in previous studies (e.g., Kollias
2 and Albrecht, 2000)..

3 Various parts of the analysis were complicated, or even hindered, by the great variability
4 observed between cases. Seasonal differences and air mass origin are likely to have a
5 strong influence on this aspect. They should be studied further to understand better their
6 impacts. For the moment, it is difficult to know the aerosol source and content in each
7 cloud, especially when the MBL has a decoupled structure.

8

9

1 **6. REFERENCES**

2

3 Abel, S. J., D. N. Walters, and G. Allen, 2010: Evaluation of stratocumulus cloud
4 prediction in the Met Office forecast model during VOCALS-REx. *Atmos. Chem.*
5 *Phys.*, **10**, 10541–10559, doi:10.5194/acp-10-10541-2010.

6

7 Albrecht, B. A., C. S. Bretherton, D. W. Johnson, W. H. Schubert, and A. S. Frisch,
8 1995: The Atlantic Stratocumulus Transition Experiment—ASTEX. *Bull. Amer.*
9 *Meteor. Soc.*, **76**, 889–904.

10

11 Augstein, E., H. Schmidt, and F. Ostapoff, 1974: The vertical structure of the
12 atmospheric planetary boundary layer in undisturbed trade winds over the Atlantic
13 Ocean. *Bound.-Layer Meteor.*, **6**, 129–150.

14

15 Bony, S., and J.-L. Dufresne, 2005: Marine boundary layer clouds at the heart of tropical
16 cloud feedback uncertainties in climate models. *Geophys. Res. Lett.*, **32**, L20806,
17 doi:10.1029/2005GL023851.

18

19 Bretherton, C. S., T. Uttal, C. W. Fairall, S. Yuter, R. Weller, D. Baumgardner, K.
20 Comstock, R. Wood, and G. Raga, 2004: The EPIC 2001 stratocumulus study. *Bull.*
21 *Amer. Meteor. Soc.*, **85**, 967–977.

22

23 Caldwell, P., C. S. Bretherton, and R. Wood, 2005: Mixed-layer budget analysis of the

1 diurnal cycle of entrainment in Southeast Pacific stratocumulus. *J. Atmos. Sci.*, **62**,
2 3775–3791.

3

4 Carman, J. K., D. L. Rossiter, D. Khelif, H. H. Jonsson, I. C. Faloona, and P. Y. Chuang,
5 2012: Observational constraints on entrainment and the entrainment interface layer in
6 stratocumulus. *Atmos. Chem. Phys. Discuss.*, **12**, 817–868. doi:10.5194/acpd-12-817-
7 2012.

8

9 Clothiaux, E. E., M. A. Miller, B. A. Albrecht, T. P. Ackerman, J. Verlinde, D. M. Babb,
10 R. M. Peters, and W. J. Syrett, 1995: An evaluation of a 94-GHz radar for remote
11 sensing of cloud properties. *J. Atmos. and Oceanic Technol.*, **12**, 201–229.

12

13 Comstock, K. K., R. Wood, S. E. Yuter, and C. S. Bretherton, 2004: Reflectivity and rain
14 rate in and below drizzling stratocumulus. *Q. J. R. Meteorol. Soc.*, **130**, 2891–2918.

15

16 de Laat, A. T. J., and P. Duynkerke, 1998: Analysis of ASTEX-stratocumulus
17 observational data using a mass-flux approach. *Bound.-Layer Meteor.*, **86**, 63–87.

18

19 de Roode, S. R., and P. G. Duynkerke, 1997: Observed Lagrangian transition of
20 stratocumulus into cumulus during ASTEX: Mean state and turbulence structure. *J.*
21 *Atmos. Sci.*, **54**, 2157–2173.

22

23 de Szoeke, S. P., and S.-P. Xie, 2008: The Tropical Eastern Pacific Seasonal Cycle:

- 1 Assessment of Errors and Mechanisms in IPCC AR4 Coupled Ocean–Atmosphere
2 General Circulation Models. *J. Clim.*, **21**, 2573–2590.
- 3
- 4 Faloon, I., D. H. Lenschow, T. Campos, B. Stevens, M. van Zanten, B. Blomquist, D.
5 Thornton, A. Bandy, and H. Gerber, 2005: Observations of entrainment in eastern
6 Pacific marine stratocumulus using three conserved scalars. *J. Atmos. Sci.*, **62**, 3268–
7 3285.
- 8
- 9 Ghatge, V. P., B. A. Albrecht, C. W. Fairall, and R. A. Weller, 2009: Climatology of
10 surface meteorology, surface fluxes, cloud fraction, and radiative forcing over the
11 Southeast Pacific from buoy observations. *J. Clim.*, **22**, 5527–5540.
- 12
- 13 Ghatge, V. P., B. A. Albrecht, and P. Kollias, 2010: Vertical velocity structure of
14 nonprecipitating continental boundary layer stratocumulus clouds. *J. Geophys. Res.*,
15 **115**, D13204, doi:10.1029/2009JD013091.
- 16
- 17 Ghatge, V. P., M. A. Miller, and L. DiPreto, 2011: Vertical velocity structure of marine
18 boundary layer trade wind cumulus clouds. *J. Geophys. Res.*, **116**, D16206,
19 doi:10.1029/2010JD015344.
- 20
- 21 Garstang, M., and A. K. Betts, 1974: A review of the tropical boundary layer and
22 cumulus convection: Structure, parameterization and modeling. *Bull. Amer. Meteor.*
23 *Soc.*, **55**, 1195–1205.

1

2 Guo, H., Y. Liu, P. H. Daum, G. I. Senum, and W. Tao, 2008: Characteristics of vertical
3 velocity in marine stratocumulus: comparison of large eddy simulations with
4 observations. *Environ. Res. Let.*, **3**, doi:10.1088/1748-9326/3/4/04520.

5

6 Harrison, E. F., P. Minnis, B. R. Barkstrom, V. Ramanathan, R. D. Cess, and G. G.
7 Gibson, 1990: Seasonal variation of cloud radiative forcing derived from the Earth
8 Radiation Budget Experiment. *J. Geophys. Res.*, **95**, 18687–18703.

9

10 Hasanean, H. M., 2004: Variability of the North Atlantic subtropical high and
11 associations with tropical sea-surface temperature. *Int. J. Climatol.*, **24**, 945–957.

12

13 Hignett, P., 1991: Observations of diurnal variation in a cloud-capped marine boundary
14 layer. *J. Atmos. Sci.*, **48**, 1474–1482.

15

16 Illingworth, A. J., R. J. Hogan, E. J. O'Connor, D. Bouniol, M. E. Brooks, J. Delanoe, D.
17 P. Donovan, J. D. Eastment, N. Gaussiat, J. W. F. Goddard, M. Haeffelin, H. Klein
18 Baltink, O. A. Krasnov, J. Pelon, J.-M. Piriou, A. Protat, H. W. J. Russchenberg, A.
19 Seifert, A. M. Tompkins, G.-J. van Zadelhoff, F. Vinit, U. Willen, D. R. Wilson and
20 C. L. Wrench, 2007: Cloudnet: Continuous evaluation of cloud profiles in seven
21 operational models using ground-based observations. *Bull. Amer. Meteor. Soc.*, **88**,
22 883–898, doi:10.1175/BAMS-88-6-883.

23

- 1 Intrieri, J. M., M. D. Shupe, T. Uttal, and B. J. McCarty, 2002: An annual cycle of Arctic
2 cloud characteristics observed by radar and lidar at SHEBA. *J. Geophys. Res.*, **107**,
3 C10, doi:10.1029/2000JC000423.
4
- 5 Klein, S. A., and D. L. Hartmann, 1993: The seasonal cycle of low stratiform clouds. *J.*
6 *Clim.*, **6**, 1587–1606.
7
- 8 Kollias, P., and B. Albrecht, 2000: The turbulence structure in a continental
9 stratocumulus cloud from millimeter-wavelength radar observations. *J. Atmos. Sci.*,
10 **57**, 2417–2434.
11
- 12 Kollias, P., B. A. Albrecht, R. Lhermitte, and A. Savtchenko, 2001: Radar observations
13 of updrafts, downdrafts, and turbulence in fair-weather cumuli. *J. Atmos. Sci.*, **58**,
14 1750–1766.
15
- 16 Kollias, P., E. E. Clothiaux, M. A. Miller, E. P. Luke, K. L. Johnson, K. P. Moran, K. B.
17 Widener, and B. A. Albrecht, 2007a: The Atmospheric Radiation Measurement
18 program cloud profiling radars: Second-generation sampling strategies, processing,
19 and cloud data products. *J. Atmos. Oceanic Technol.*, **24**, 1199–1214,
20 doi:10.1175/JTECH2033.1.
21
- 22 Kollias, P., G. Tselioudis, and B. A. Albrecht, 2007b: Cloud climatology at the Southern
23 Great Plains and the layer structure, drizzle, and atmospheric modes of continental

1 stratus. *J. Geophys. Res.*, **112**, D09116, doi:10.1029/2006JD007307.

2

3 Kollias, P., J. Rémillard, E. Luke, and W. Szyrmer, 2011a: Cloud radar Doppler spectra
4 in drizzling stratiform clouds: Part 1. Forward modeling and applications. *J. Geophys.*
5 *Res.*, **116**, doi:10.1029/2010JD015237.

6

7 Kollias, P., W. Szyrmer, J. Rémillard, and E. Luke, 2011b: Cloud radar Doppler spectra
8 in drizzling stratiform clouds: Part 2. Observations and microphysical modeling of
9 drizzle evolution, *J. Geophys. Res.*, **116**, doi:10.1029/2010JD015238.

10

11 Kubar, T. L., D. L. Hartmann, and R. Wood, 2009: Understanding the importance of
12 microphysics and macrophysics for warm rain in marine low clouds. Part I: Satellite
13 observations. *J. Atmos. Sci.*, **66**, 2953–2972.

14

15 Kuo, H.-C., and W. H. Schubert, 1988: Stability of cloud-topped boundary layers. *Q. J.*
16 *R. Meteorol. Soc.*, **114**, 887–916.

17

18 Lhermitte, R., 1990: Attenuation and scattering of millimeter wavelength radiation by
19 clouds and precipitation. *J. Atmos. Oceanic Technol.*, **7**, 464–479.

20

21 Liljegren, J. C., 1994: Two-channel microwave radiometer for observations of total
22 column precipitable water vapor and cloud liquid water path. Paper presented at the
23 Fifth Symposium on Global Change Studies, Am. Meteorol. Soc., Nashville, Tenn,

1 262–269.

2

3 Liu, Z., M. Vaughan, D. Winker, C. Kittaka, B. Getzewich, R. Kuehn, A. Omar, K.
4 Powell, C. Trepte, and C. Hostetler, 2009: The CALIPSO lidar cloud and aerosol
5 discrimination: Version 2 algorithm and initial assessment of performance. *J. Atmos.*
6 *Oceanic Technol.*, **26**, 1198–1213, doi:10.1175/2009JTECHA1229.1.

7

8 Lothon, M., D. H. Lenschow, D. Leon, and G. Vali, 2005: Turbulence measurement in
9 marine stratocumulus with Doppler radar. *Quart. J. Roy. Meteor. Soc.*, **131**, 2063–
10 2080.

11

12 Luke, E. P., P. Kollias, and M. D. Shupe, 2010: Detection of supercooled liquid in mixed-
13 phase clouds using radar Doppler spectra. *J. Geophys. Res.*, **115**, D19201,
14 doi:10.1029/2009JD012884.

15

16 MacVean, M. K., and P. J. Mason, 1990: Cloud-top entrainment instability through
17 small-scale mixing and its parameterization in numerical models. *J. Atmos. Sci.*, **47**,
18 1012–1030.

19

20 Markowicz, K. M., P. J. Flatau, A. E. Kardas, J. Remiszewska, K. Stelmaszczyk, and L.
21 Woeste, 2008: Ceilometer retrieval of the boundary layer vertical aerosol extinction
22 structure. *J. Atmos. Oceanic Technol.*, **25**, 928–944, doi:10.1175/2007JTECHA1016.1.

23

- 1 Mead, J. B., and K. B. Widener, 2005: W-band ARM cloud radar. Preprints. *32nd Int.*
2 *Conf. on Radar Meteorology*, Albuquerque, NM, Amer. Meteor. Soc., CD-ROM,
3 P1R.3.
4
- 5 Münkkel, C., N. Eresmaa, J. Räsänen, and A. Karppinen, 2007: Retrieval of mixing height
6 and dust concentration with lidar ceilometer. *Bound.-Layer Meteor.*, **124**, 117–128.
7
- 8 Nicholls, S., 1989: The structure of radiatively driven convection in stratocumulus. *Q. J.*
9 *R. Meteorol. Soc.*, **115**, 487–511.
10
- 11 Norris, J. R., and S. A. Klein, 2000: Low cloud type over the ocean from surface
12 observations. Part III: Relationship to vertical motion and the regional surface synoptic
13 environment. *J. Clim.*, **13**, 245–256.
14
- 15 O'Connor, E. J., R. J. Hogan, and A. J. Illingworth, 2005: Retrieving stratocumulus
16 drizzle parameters using Doppler radar and lidar. *J. Appl. Meteorol.*, **44**, 14–27.
17
- 18 Ramanathan, V., R. D. Cess, E. F. Harrison, P. Minnis, B. R. Barkstrom, E. Ahmad, and
19 D. Hartmann, 1989: Cloud-radiative forcing and climate: Results from the Earth
20 Radiation Budget Experiment. *Science*, **243**, 57–63.
21
- 22 Randall, D. A., J. A. Coakley Jr., D. H. Lenschow, C. W. Fairall, and R. A. Kropfli,
23 1984: Outlook for research on subtropical marine stratiform clouds. *Bull. Amer.*

- 1 *Meteor. Soc.*, **65**, 1290–1301.
- 2
- 3 Randall, D. A., Q. Shao, and C.-H. Moeng, 1992: A second-order bulk boundary-layer
4 model. *J. Atmos. Sci.*, **49**, 1903–1923.
- 5
- 6 Rozendaal, M. A., C. B. Leovy, and S. A. Klein, 1995: An observational study of diurnal
7 variations of marine stratiform cloud. *J. Clim.*, **8**, 1795–1809.
- 8
- 9 Serpetzoglou, E., B. A. Albrecht, P. Kollias, and C. W. Fairall, 2008: Boundary layer,
10 cloud, and drizzle variability in the southeast Pacific stratocumulus regime. *J. Clim.*,
11 **21**, 6191–6214.
- 12
- 13 Stevens, B., 2007: On the growth of layers of nonprecipitating cumulus convection. *J.*
14 *Atmos. Sci.*, **64**, 2916–2931.
- 15
- 16 Stevens, B., C.-H. Moeng, and P. P. Sullivan, 1999: Large-eddy simulations of
17 radiatively driven convection: sensitivities to the representation of small scales. *J.*
18 *Atmos. Sci.*, **56**, 3963–3984.
- 19
- 20 Stevens, B., D. H. Lenschow, G. Vali, H. Gerber, A. Bandy, B. Blomquist, J.-L.
21 Brenguier, C. S. Bretherton, F. Burnet, T. Campos, S. Chai, I. Faloon, D. Friesen, S.
22 Haimov, K. Laursen, D. K. Lilly, S. M. Loehrer, S. P. Malinowski, B. Morley, M. D.
23 Petters, D. C. Rogers, L. Russell, V. Savic-Jovicic, J. R. Snider, D. Straub, M. J.

- 1 Szumowski, H. Takagi, D. C. Thornton, M. Tschudi, C. Twohy, M. Wetzel, and M. C.
2 van Zanten, 2003: Dynamics and chemistry of marine stratocumulus—DYCOMS-II.
3 *Bull. Amer. Meteor. Soc.*, **84**, 579–593, doi:10.1175/BAMS-84-5-579.
- 4
- 5 Ulaby, F. T., R. K. Moore, and A. K. Fung, 1981: *Microwave remote sensing: Active and*
6 *passive. Vol. 1, Microwave remote sensing fundamentals and radiometry*, Addison-
7 Wesley, 456 pp.
- 8
- 9 Wang, J., and W. B. Rossow, 1995: Determination of cloud vertical structure from upper-
10 air observations. *J. Appl. Meteorol.*, **34**, 2243–2258.
- 11
- 12 Wood, R., 2005: Drizzle in stratiform boundary layer clouds. Part I: Vertical and
13 horizontal structure. *J. Atmos. Sci.*, **62**, 3011–3033.
- 14
- 15 Wood, R., and C. S. Bretherton, 2004: Boundary layer depth, entrainment, and decoupling
16 in the cloud-capped subtropical and tropical marine boundary layer. *J. Clim.*, **17**,
17 3576–3588.
- 18
- 19 Wood, R., and C. S. Bretherton, 2006: On the relationship between stratiform low cloud
20 cover and lower tropospheric stability. *J. Clim.*, **19**, 6425–6432.
- 21
- 22 Wood, R., C. S. Bretherton, and D. L. Hartmann, 2002: Diurnal cycle of liquid water path
23 over the subtropical and tropical oceans. *Geophys. Res. Lett.*, **29**, 2092,

1 doi:10.1029/2002GL015371.

2

3 Wood, R., C. R. Mechoso, C. S. Bretherton, R. A. Weller, B. Huebert, F. Straneo, B. A.
4 Albrecht, H. Coe, G. Allen, G. Vaughan, P. Daum, C. Fairall, D. Chand, L. Gallardo
5 Klenner, R. Garreaud, C. Grados, D. S. Covert, T. S. Bates, R. Krejci, L. M. Russell,
6 S. de Szoeke, A. Brewer, S. E. Yuter, S. R. Springston, A. Chaigneau, T. Toniazzo, P.
7 Minnis, R. Palikonda, S. J. Abel, W. O. J. Brown, S. Williams, J. Fochesatto, J.
8 Brioude, and K. N. Bower, 2011: The VAMOS Ocean-Cloud-Atmosphere-Land Study
9 Regional Experiment (VOCALS-REx): goals, platforms, and field operations. *Atmos.*
10 *Chem. Phys.*, **11**, 627–654, doi:10.5194/acp-11-627-2011.

11

12 Yamagushi, T., and D. A. Randall, 2008: Large-eddy simulation of evaporatively driven
13 entrainment in cloud-topped mixed layers. *J. Atmos. Sci.*, **65**, 1481–1504.

14

15 Yin, B., and B. A. Albrecht, 2000: Spatial variability of atmospheric boundary layer
16 structure over the eastern equatorial Pacific. *J. Clim.*, **13**, 1574–1592.

17

18 Zhang, G. J., A. M. Vogelmann, M. P. Jensen, W. D. Collins, and E. P. Luke, 2010:
19 Relating satellite-observed cloud properties from MODIS to meteorological conditions
20 for marine boundary layer clouds. *J. Clim.*, **23**, 1374–1391,
21 doi:10.1175/2009JCLI2897.1.

22

23 Zuidema, P., E. R. Westwater, C. Fairall, and D. Hazen, 2005: Ship-based liquid water

1 path estimates in marine stratocumulus. *J. Geophys. Res.*, **110**, D20206,
2 doi:10.1029/2005JD005833.

3

1 7. FIGURE CAPTION

2

3 Fig. 1 Monthly statistics of good running time for the WACR (black), ceilometer (dark
4 gray), and MWR (light gray). Operations are considered bad when more than a minute
5 separates successive measurements. Note that the radar started working in early June
6 2009, and it was down for about 23 days in September 2010. Note also that the
7 radiometer measurements from July 11, 2010 through August 9, 2010 are unreliable, due
8 to a software problem, although it is not shown here. The numbers above the graph
9 represent the number of soundings taken during each month that returned good
10 measurements.

11 Fig. 2 Top: True color images from MODIS on board Terra taken around 1315UTC, and
12 spanning about 500km in both dimensions centered at the location of Graciosa Island
13 (shown in red circle). The left image shows a stratocumulus cloud case (November 22,
14 2009) and the right image shows a broken cumulus (03:00-06:00 UTC) and cumulus with
15 stratocumulus (18:00-24:00 UTC) cases (August 30, 2010). Bottom: The corresponding
16 daily WACR time-height reflectivity observations with the first ceilometer cloud base
17 shown as black dots.

18 Fig. 3 Monthly statistics of (a) cloud and liquid precipitation coverage using the lidar-
19 radar algorithm, (b) the four main cloud types, (c) low-level clouds, and (d) liquid
20 precipitation types. Note that the September 2010 results come from only 8 days due to a
21 radar downtime. Also note that the precipitation reported here relates to the first cloud
22 layer only. (e) Time series of LTS as retrieved from the radiosondes launches.

1 Fig. 4 a) Distributions of the hourly cloud base heights for the stratocumulus and cumulus
2 clouds (respectively the black and gray lines). b) Distributions of the distance between
3 the transition layer and the cumulus hourly base (gray line), and between the
4 stratocumulus hourly top and the inversion layer (black line).

5 Fig. 5 Monthly statistics of (a) the transition and inversion layers base height, and the
6 stratocumulus clouds boundaries, and (b) the occurrences of the inversion and transition
7 layers, as a fraction of the number of soundings per month.

8 Fig. 6 Daily (a) and annual (b) cycles of hours characterized by single and multi-layer
9 clouds in the MBL (respectively the gray and black bars). Each number of occurrences is
10 normalized by the total number of hours with data within the considered hour (a) or
11 month (b), to provide percentage values. Note that the local standard time in the Azores is
12 UTC-1h.

13 Fig. 7 Profiles of (a) potential temperature (black; bottom axis) and water vapor mixing
14 ratio (gray; top axis), (b) wind speed, (c) wind direction, and (d) relative humidity
15 composited over the cases with multiple BL clouds (dash-dotted lines), a single BL cloud
16 at the inversion or transition level (solid and dashed lines respectively), all presenting a
17 transition layer.

18 Fig. 8 Distribution of instantaneous cloud base (a) and depth (b), LWP (c), inversion
19 depth (d) and strengths (e), and transition strength (f) measured in the selected
20 stratocumulus cases. In (a)-(c), measurements were divided according to the absence or
21 presence of a drizzle shaft (respectively the black and gray curves). In (e), the strength is
22 reported in terms of equivalent potential temperature (black curve), and in terms of water

1 vapor mixing ratio (gray curve). In (f), the vertical dashed line corresponds to the
2 minimum value used to detect a transition layer (based on Yin and Albrecht, 2000).

3 Fig. 9 3-hourly statistics, composited from 35 days of persisting single-layer
4 stratocumulus coverage, separated between periods without radar echoes below the cloud
5 base and periods with various types of drizzle (virga, light, or intense): (a) fraction of the
6 stratocumulus coverage, (b) cloud base (dashed) and top (solid) heights, (c) cloud depth,
7 and (d) LWP from the MWR. The average stratocumulus coverage is also included in (a)
8 with the thick line. The error bars in (c-d) represent the standard deviations.

9 Fig. 10 Night (solid) and day (dashed) average profiles of the hourly-estimated variance
10 and skewness of the radar measured mean Doppler velocity (a and c respectively), and 3-
11 hourly profiles of the variance and skewness of the radar measured mean Doppler
12 velocity (b and d respectively), composited over the selected periods of stratocumulus
13 without drizzle under the cloud base. Note that the vertical axis represents the height
14 above cloud base, in units of cloud depths, thus covering only the cloud layer.

15 Fig. 11 Night (black) and day (gray) profiles of (a) updraft and downdraft velocities, (b)
16 updraft area, and (c) mass flux associated with the updrafts, as obtained using three
17 methods: direct sampling (solid lines), coherent structures only (short dashes), and the
18 statistical method (long dashes).

19

20

1 **Table 1a:** List of liquid precipitation types and their main characteristics used to
 2 differentiate them.

Type	Virga	Light	Intense
Echo base	> 200m	< 200m	< 200m
Base reflectivity	—	< 0dBZ	≥ 0dBZ
Echo below CB	Yes	Yes	Possible

3

4

5 **Table 1b:** List of cloud types and their main characteristics used to differentiate them in
 6 the identification algorithm. The last row indicates the type of precipitation most likely
 7 associated with each cloud type.

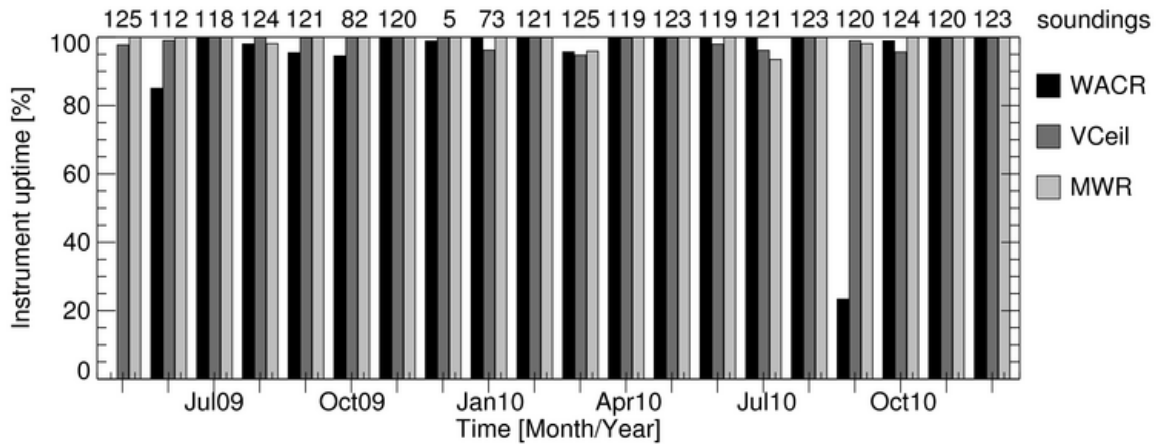
Type → Characteristic ↓	High	Middle	Low			Deep BL
			Cu	Sc	indeterm.	
Cloud base	> 7km	> 3km	—	—	—	≤ 3km
Cloud top	—	—	≤ 3km	≤ 3km	≤ 3km	> 3km
Duration	—	—	< 20min	≥ 20min	≥ 20min	—
CT variability	—	—	—	< 100m	≥ 100m	—
Type of precip	—	virga	virga	light	intense	intense

8

9

10

1



2

3 Fig. 1 Monthly statistics of good running time for the WACR (black), ceilometer (dark
 4 gray), and MWR (light gray). Operations are considered bad when more than a minute
 5 separates successive measurements. Note that the radar started working in early June
 6 2009, and it was down for about 23 days in September 2010. Note also that the
 7 radiometer measurements from July 11, 2010 through August 9, 2010 are unreliable,
 8 due to a software problem, although it is not shown here. The numbers above the graph
 9 represent the number of soundings taken during each month that returned good
 10 measurements.

11

12

13

14

15

16

17

18

19

20

21

22

23

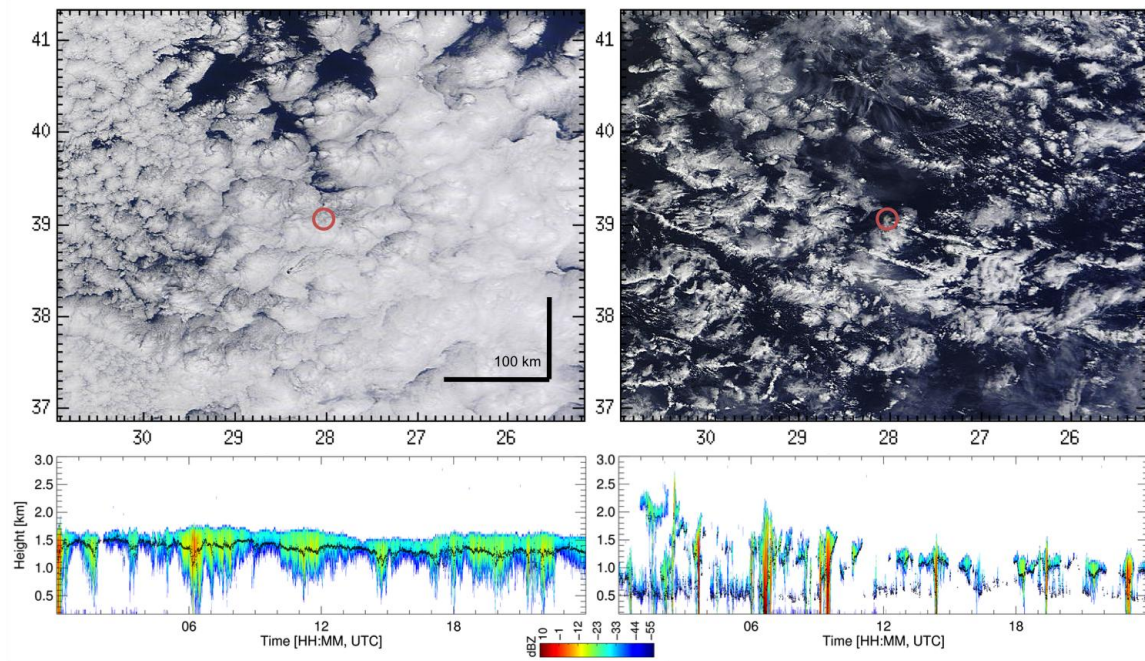
24

25

26

27

1



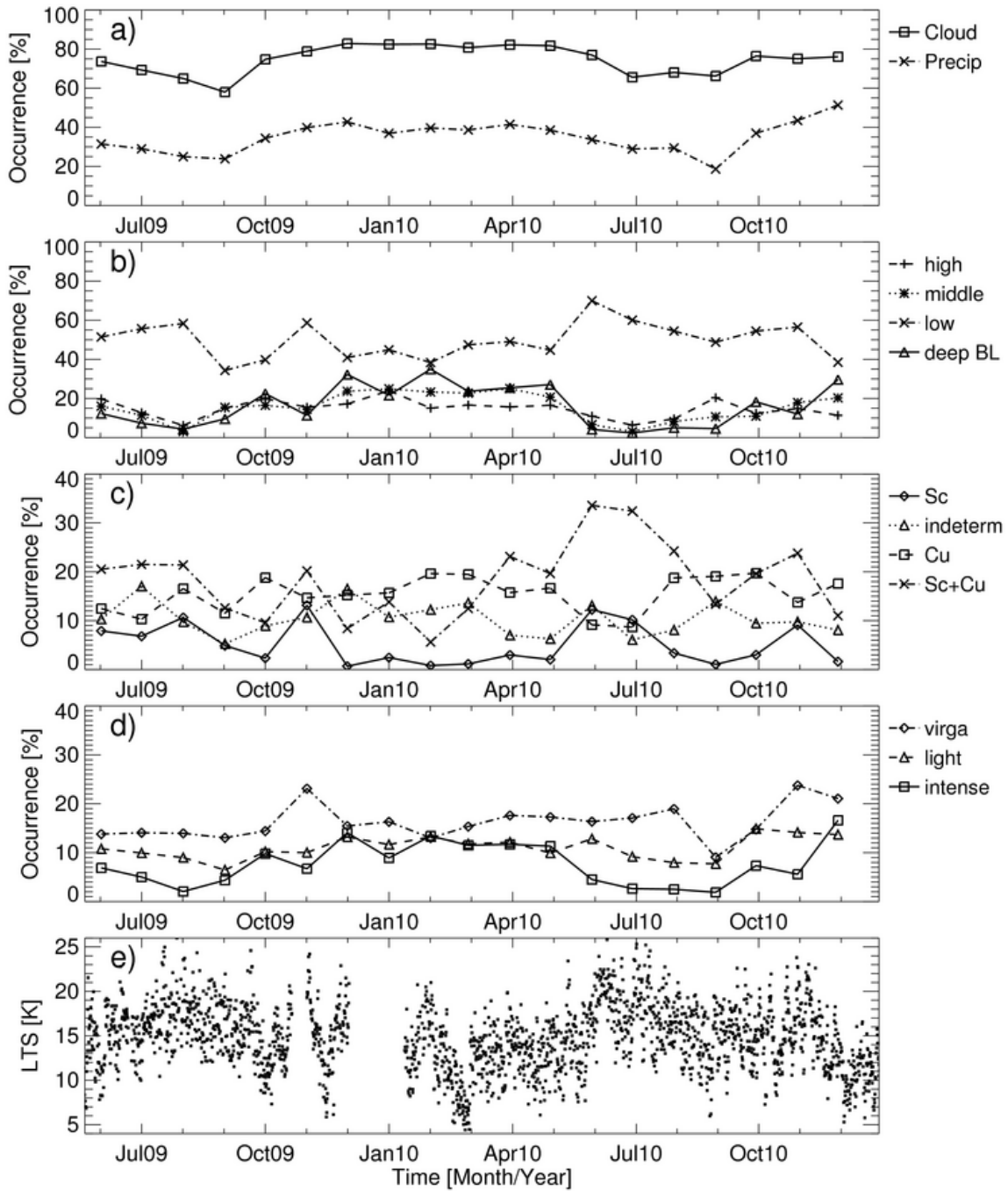
2

3

4

5 Fig. 2 Top: True color images from MODIS on board Terra taken around 1315UTC, and
 6 spanning about 500km in both dimensions centered at the location of Graciosa Island
 7 (shown in red circle). The left image shows a stratocumulus cloud case (November 22,
 8 2009) and the right image shows a broken cumulus (18:00-24:00 UTC) cases (August 30,
 9 2010). Bottom: The corresponding daily WACR time-height reflectivity observations
 10 with the first ceilometer cloud base shown as black dots.

11

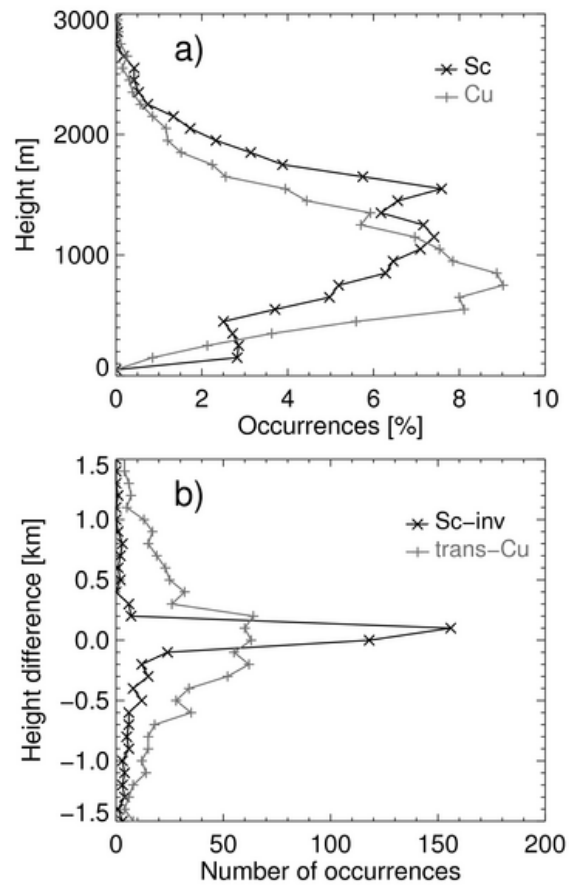


1

2 Fig. 3 Monthly statistics of (a) cloud and liquid precipitation coverage using the lidar-
 3 radar algorithm, (b) the four main cloud types, (c) low-level clouds, and (d) liquid
 4 precipitation types. Note that the September 2010 results come from only 8 days due to a
 5 radar downtime. Also note that the precipitation reported here relates to the first cloud
 6 layer only. (e) Time series of LTS as retrieved from the radiosondes launches.

7

8

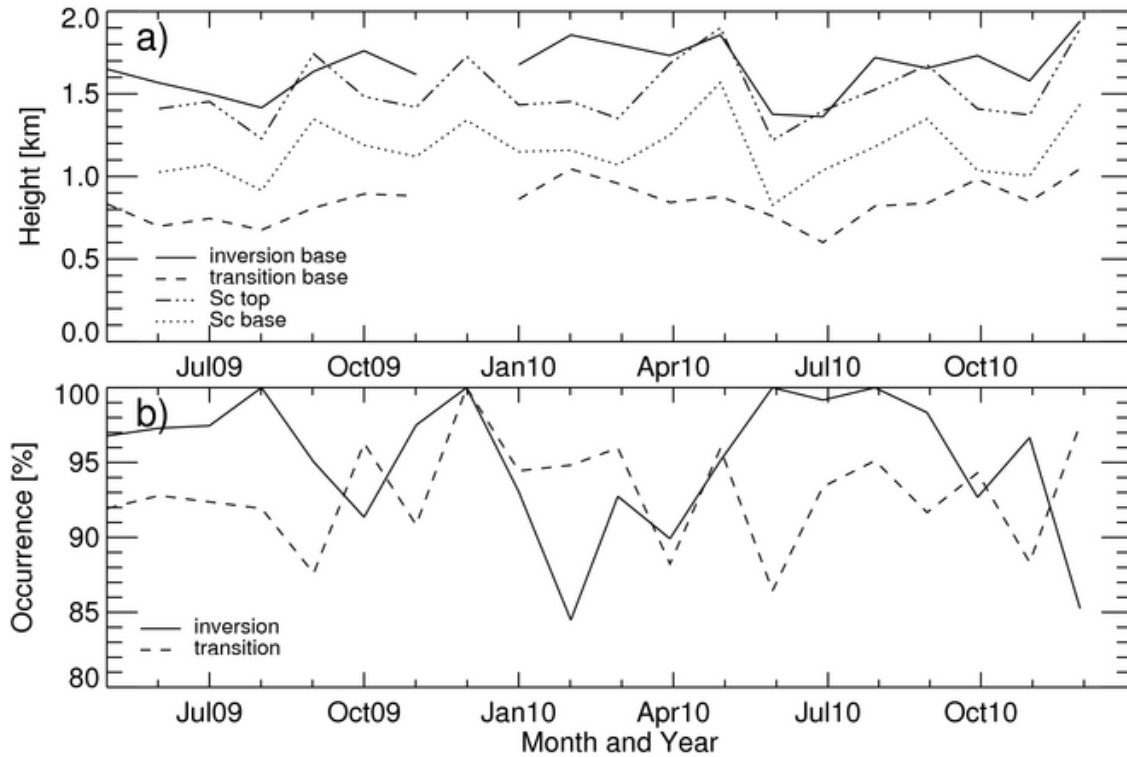


1

2 Fig. 4 a) Distributions of the hourly cloud base heights for the stratocumulus and cumulus
 3 clouds (respectively the black and gray lines). b) Distributions of the distance between
 4 the transition layer and the cumulus hourly base (gray line), and between the
 5 stratocumulus hourly top and the inversion layer (black line).

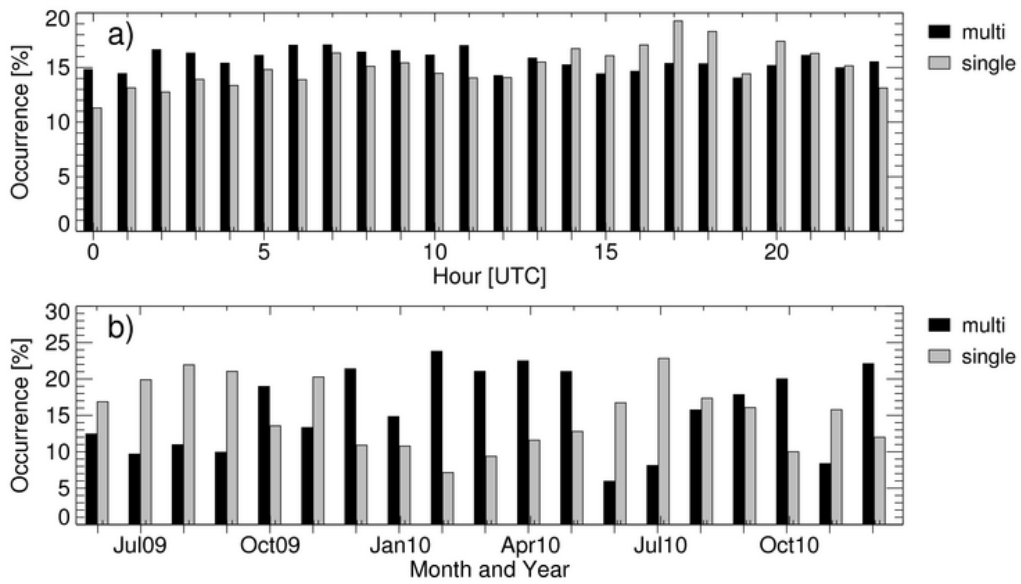
6

7



1
2
3
4
5
6

Fig. 5 Monthly statistics of (a) the transition and inversion layers base height, and the stratocumulus clouds boundaries, and (b) the occurrences of the inversion and transition layers, as a fraction of the number of soundings per month.

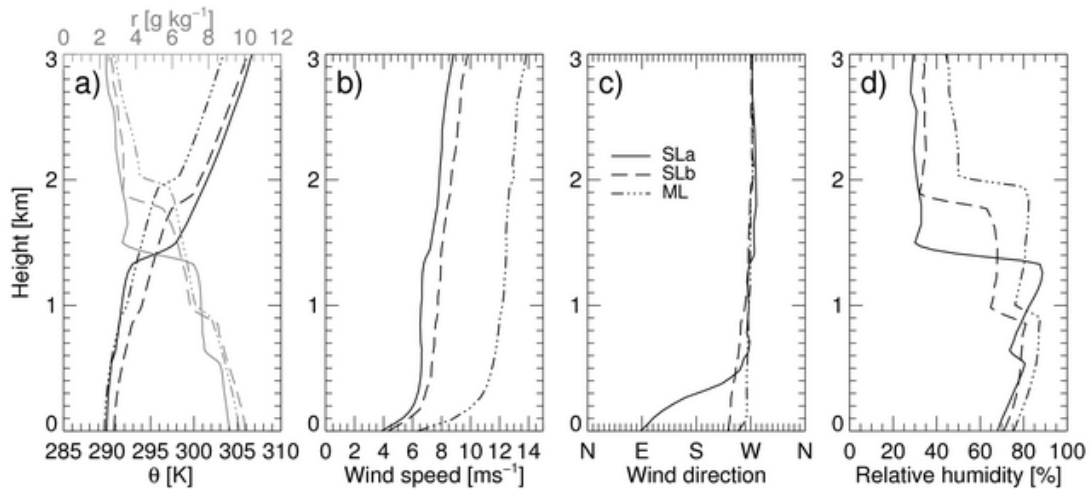


1

2 Fig. 6 Daily (a) and annual (b) cycles of hours characterized by single and multi-layer
 3 clouds in the MBL (respectively the gray and black bars). Each number of occurrences is
 4 normalized by the total number of hours with data within the considered hour (a) or
 5 month (b), to provide percentage values. Note that the local standard time in Azores is
 6 UTC-1h.

7

8

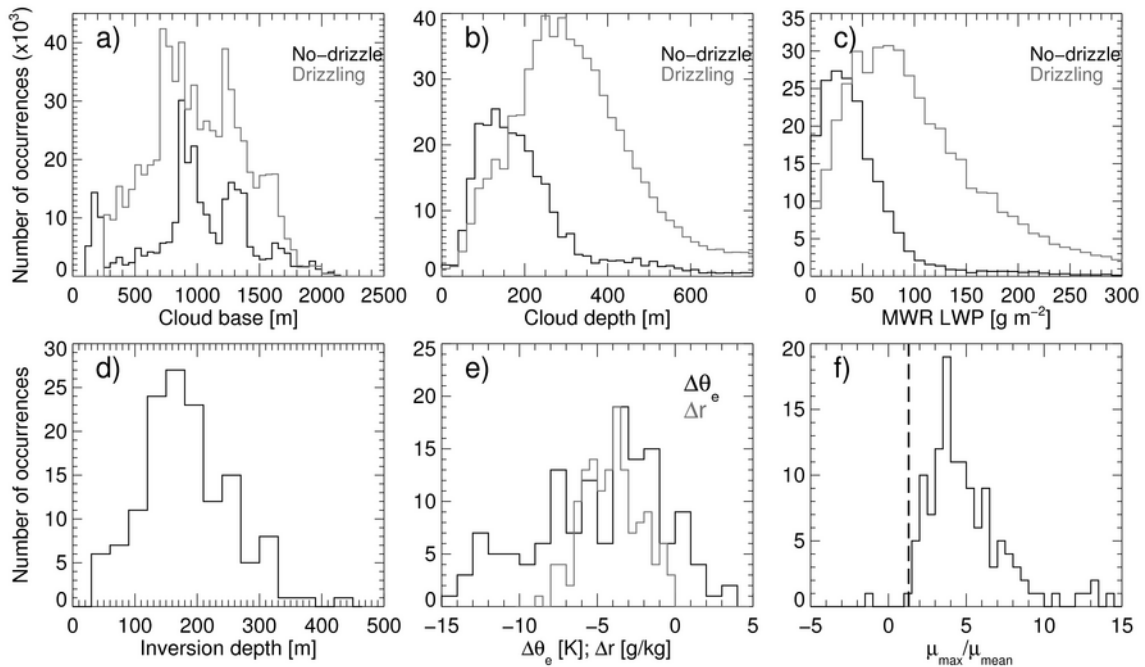


1

2 Fig. 7 Profiles of (a) potential temperature (black; bottom axis) and water vapor mixing
 3 ratio (gray; top axis), (b) wind speed, (c) wind direction, and (d) relative humidity
 4 composited over the cases with multiple BL clouds (dash-dotted lines), a single BL cloud
 5 at the inversion or transition level (solid and dashed lines respectively), all presenting a
 6 transition layer.

7

8

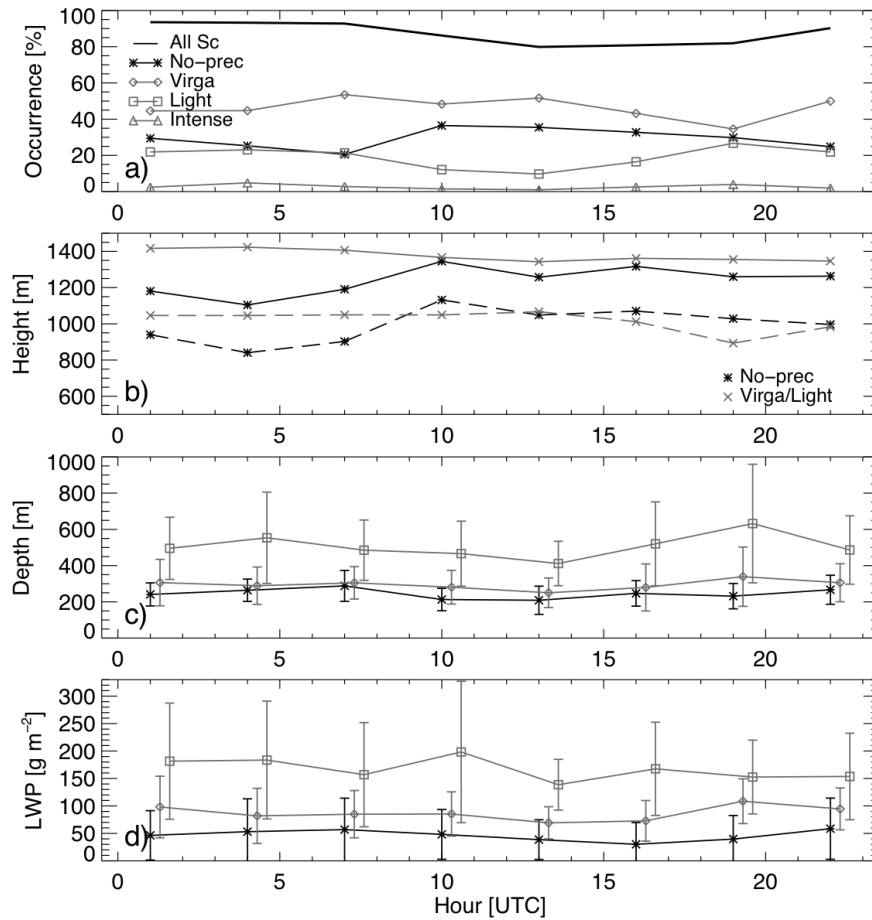


1

2 Fig. 8 Distribution of instantaneous cloud base (a) and depth (b), LWP (c), inversion
 3 depth (d) and strengths (e), and transition strength (f) measured in the selected
 4 stratocumulus cases. In (a)-(c), measurements were divided according to the absence or
 5 presence of a drizzle shaft (respectively the black and gray curves). In (e), the strength is
 6 reported in terms of equivalent potential temperature (black curve), and in terms of water
 7 vapor mixing ratio (gray curve). In (f), the vertical dashed line corresponds to the
 8 minimum value used to detect a transition layer (based on Yin and Albrecht, 2000).

9

10

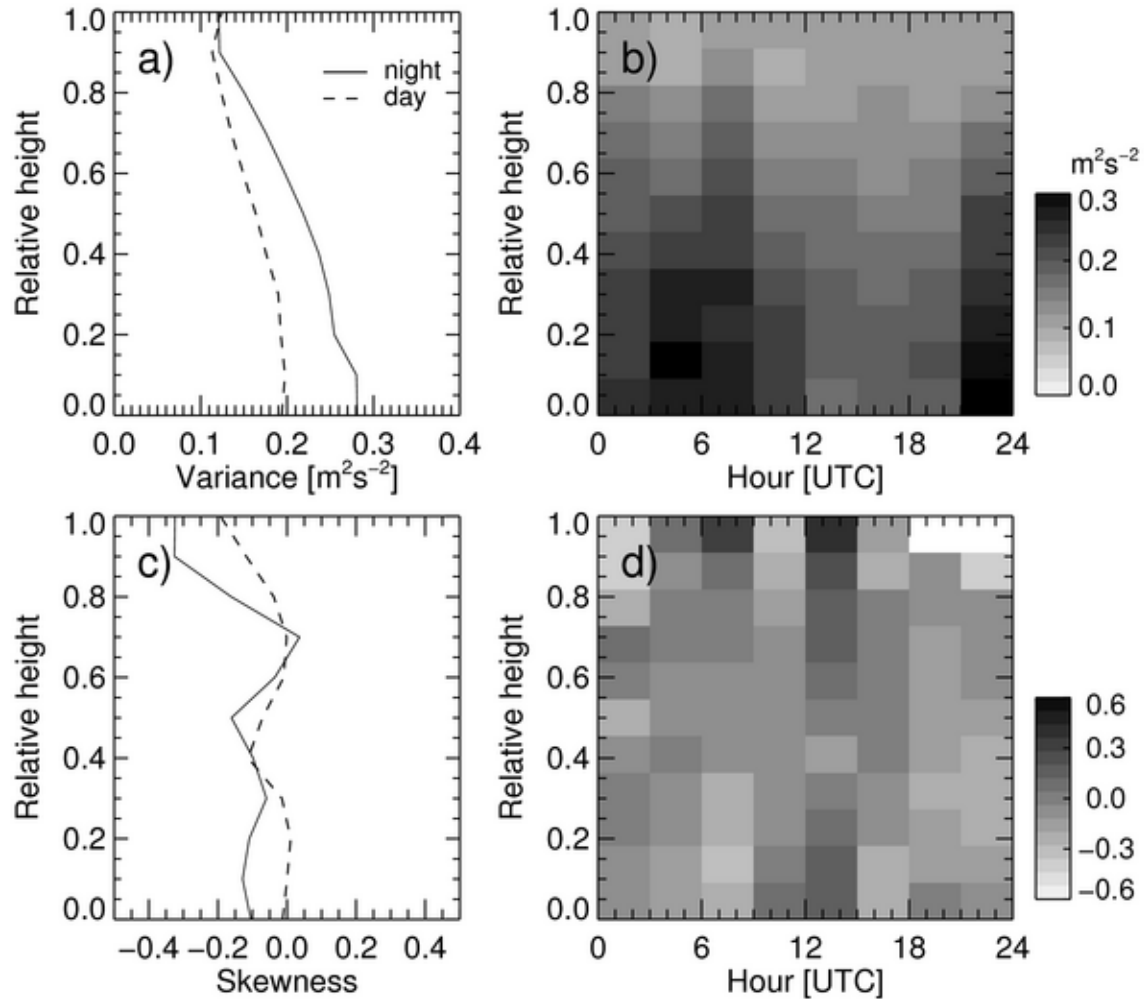


1

2 Fig. 9 3-hourly statistics, composited from 35 days of persisting single-layer
 3 stratocumulus coverage, separated between periods without radar echoes below the cloud
 4 base and periods with various types of drizzle (virga, light, or intense): (a) fraction of the
 5 stratocumulus coverage, (b) cloud base (dashed) and top (solid) heights, (c) cloud depth,
 6 and (d) LWP from the MWR. The average stratocumulus coverage is also included in (a)
 7 with the thick line. The error bars in (c-d) represent the standard deviations.

8

9



1

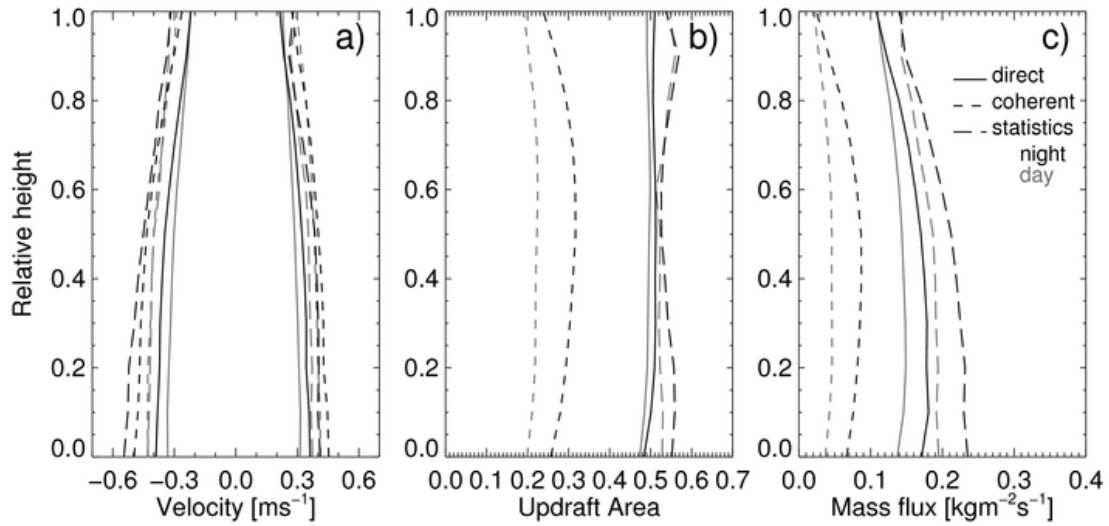
2

3 Fig. 10 Night (solid) and day (dashed) average profiles of the hourly-estimated variance
 4 and skewness of the radar measured mean Doppler velocity (a and c respectively), and 3-
 5 hourly profiles of the variance and skewness of the radar measured mean Doppler
 6 velocity (b and d respectively), composited over the selected periods of stratocumulus
 7 without drizzle under the cloud base. Note that the vertical axis represents the height
 8 above cloud base, in units of cloud depths, thus covering only the cloud layer.

9

10

11



1

2 Fig. 11 Night (black) and day (gray) profiles of (a) updraft and downdraft velocities, (b)
 3 updraft area, and (c) mass flux associated with the updrafts, as obtained using three
 4 methods: direct sampling (solid lines), coherent structures only (short dashes), and the
 5 statistical method (long dashes).

6

7

8